

**IMPACT INDUCED MICROSTRUCTURAL AND CRYSTAL
ANISOTROPY EFFECTS ON THE PERFORMANCE OF HMX BASED
ENERGETIC MATERIALS**

by
Ayotomi Olokun

A Dissertation

*Submitted to the Faculty of Purdue University
In Partial Fulfillment of the Requirements for the degree of*

Doctor of Philosophy



School of Aeronautics and Astronautics
West Lafayette, Indiana
May 2021

THE PURDUE UNIVERSITY GRADUATE SCHOOL
STATEMENT OF COMMITTEE APPROVAL

Dr. Vikas Tomar, Chair

School of Aeronautics and Astronautics

Dr. Arun Prakash

School of Civil Engineering

Dr. Pablo Zavattieri

School of Civil Engineering

Dr. Marcial Gonzalez

School of Mechanical Engineering

Approved by:

Dr. Gregory A. Blaisdell

Dedicated to my family.

ACKNOWLEDGMENTS

Firstly, I would like to thank Dr. Vikas Tomar for guiding me through this research as an adviser. It has been a great experience learning from him and working with him throughout my graduate career. Dr. Tomar has served not only as an advisor, but as an inspiration and a mentor who truly cares about the prosperity of his students. I am confident that the skills instilled in me from my time working with him will positively influence my personal and academic growth, as it already has, and I am greatly indebted to him for this.

I would sincerely like to extend my gratitude to Dr. Arun Prakash, Dr. Marcial Gonzalez, and Dr. Pablo Zavattieri, it was my honor to have them serve as my committee members. Their enthusiasm, knowledge, and expertise especially displayed during the preliminary and final examinations helped me tremendously in refining my research.

Next, I would like to thank my lab mates and alumni at the Interfacial Multiphysics Lab: Abhijeet Dhiman, Bing Li, Luis Buades, Ayush Rai, Meghana Sudarshan, Tyler Dillard, Leonardo Fachhini, Casey Jones, Nolan Lewis, Chandra Prakash, and Hao Wang. They have been my colleagues, mentors, and friends, and the support I received will always be appreciated. It has been my pleasure to have worked alongside everyone, all the experiences together, both in the lab and out, have led to the development of unexpected but great friendships. I would like to extend this sentiment to the faculty and staff in the School of Aeronautics and Astronautics.

Lastly, I would like to thank my parents, my sisters, Sungwoo Kim, and my friends for their unfailing love, support, and encouragement, without which I could not be where I am.

TABLE OF CONTENTS

ACKNOWLEDGMENTS	4
TABLE OF CONTENTS.....	5
LIST OF TABLES	7
LIST OF FIGURES	8
ABSTRACT.....	10
1. INTRODUCTION	11
1.1 Objectives	12
2. EXPERIMENTAL MEASUREMENTS OF ANISOTROPIC CONSTITUTIVE BEHAVIOR OF β -HMX CRYSTALS	15
2.1 Introduction.....	16
2.2 Methods.....	18
2.2.1 Sample Preparation.....	19
2.2.2 Anisotropic Elastic Constitutive Properties.....	21
2.2.2.1 Nanoindentation	22
2.2.2.2 Hardness and Modulus Evaluation	23
2.2.2.3 Indentation Size Effect (ISE)	24
2.2.3 Anisotropic Strain-Rate-Dependent Viscoplastic Constitutive Model.....	25
2.2.3.1 Dynamic Small-Scale Impact Experiments	25
2.2.3.2 Viscoplastic Constitutive Parameter Evaluation.....	27
2.3 Results and Discussion	28
2.4 Conclusions.....	36
3. EXPERIMENTAL MEASUREMENTS OF ANISOTROPIC FRACTURE PROPERTIES OF β -HMX CRYSTALS MEASURED BY NANOINDENTATION	37
3.1 Introduction.....	37
3.2 Methods.....	39
3.2.1 Sample Preparation.....	39
3.2.2 Nanoindentation.....	41
3.2.3 Fracture Toughness and Surface Energy	42

3.3 Results and Discussion	44
3.4 Conclusions.....	51
4. EXAMINATION OF LOCAL MICROSCALE-MICROSECOND TEMPERATURE RISE IN HMX-HTPB ENERGETIC MATERIAL UNDER IMPACT LOADING	53
4.1 Introduction.....	54
4.2 Method.....	55
4.3 Results.....	57
4.4 Conclusion	63
5. COHESIVE FINITE ELEMENT MODELING OF THE EFFECT OF PARTICLE ANISOTROPY ON THE MECHANICAL RESPONSE OF IMPACT LOADED HMX-BASED PBX MICROSTRUCTURE	65
5.1 Introduction.....	65
5.2 Method	67
5.2.1 Cohesive Finite Element Model	67
5.2.2 Material Model	69
5.3 Results and Discussion	72
5.4 Conclusions.....	79
6. SUMMARY AND CONCLUSIONS	80
6.1 Summary.....	80
6.2 Assumptions and Limitations	81
7. FUTURE WORK.....	83
PUBLICATIONS.....	85
REFEENCES	86

LIST OF TABLES

Table 2.1. Indentation moduli obtained from this work in comparison to elastic moduli presented in published works.	30
Table 2.2. Properties obtained for each tested plane of β -HMX by indentation	33
Table 2.3. Anisotropic viscoplastic parameters	34
Table 3.1. Anisotropic fracture toughness and surface energy values (Lawn's model)	50
Table 4.1. Microstructure Character of Energetic Material Crystals.....	60
Table 5.1. Mie-Gruneisen parameters for HTPB and HMX.....	69
Table 5.2. Cohesive parameters for HTPB and HMX	69
Table 5.3. Anisotropic viscoplastic parameters	70

LIST OF FIGURES

Figure 2.1. Identified faces of β -HMX crystals for two morphologies: a) and c) show morphology 1 and b) and d) show morphology 2.	20
Figure 2.2. (a) Crystallographic axes and planes of monoclinic β -HMX (b) Before and after images showing cleaving of embedded β -HMX crystal to expose (100) plane.....	21
Figure 2.3. Nanoindentation experiment setup	22
Figure 2.4. (a) Small-scale dynamic impact experiment setup (b) Load-depth plot and derived velocity-time plot from one impact experiment.....	26
Figure 2.5. Indentation load vs depth plot comparisons of different planes of β -HMX crystal ...	29
Figure 2.6. Imaged indentations performed on the (010) facet of a β -HMX crystal.	30
Figure 2.7. Anisotropic behavior of β -HMX crystal planes with respect to modulus and hardness	31
Figure 2.8. Comparisons of Nix Gao fitting of hardness data for 3 planes	32
Figure 2.9. Viscoplastic model parameters are obtained by fitting impact data to viscoplastic power law from 100 plane	33
Figure 2.10. Comparisons of exponent values in viscoplastic model.....	35
Figure 3.1. Crystallographic axes and unit cell parameters of β -HMX.....	40
Figure 3.2. Identified orientations of β -HMX crystals: a) morphology 1 b) morphology 2.....	40
Figure 3.3. Diamond Berkovich tipped conical indenter.....	41
Figure 3.4. (A) Top view of indent with radial cracks (B) Side view of indents with radial cracks.....	43
Figure 3.5. Imaged indentations performed on the (010) facet of a β -HMX crystal.....	44
Figure 3.6. Load vs crack length comparison for 3 facets	45
Figure 3.7. Slip planes and cracking along cleavage planes for indentation on (010) facet.....	46
Figure 3.8. Comparison of anisotropic fracture toughness and surface energy vs load using Laugier's model	47
Figure 3.9. Sub-surface cracks developed upon indentation loading on {011} facet.....	48
Figure 3.10. Comparison of anisotropic fracture toughness and surface energy vs load using Lawn's model.....	49
Figure 3.11. Comparison of Fracture toughness vs $P/c^{3/2}$ for both models	51
Figure 4.1. Experimental Setup. Left: drop hammer impact setup, right: infrared camera setup for temperature acquisition.....	56

Figure 4.2. (a): Temperature map of HMX particle ignition under impact with HMX particle profile: ignition initiation ($t=0.02$ s, $t=0$ s for hammer impact), ignition ($t=0.15$ s) and post ignition ($t=0.49$ s); (b): Post impact interface debonding of crystal 1; (c): Post impact fracture of crystal 2.	59
Figure 4.3. Temperature-time profile of impact showing different channels in different colors .	62
Figure 4.4. Location of the temperature maps on the time profile	63
Figure 5.1. Finite element model showing boundary condition, loading configuration, and cross triangle mesh.	68
Figure 5.2. Microstructure for a) isotropic material property model of HMX particles b) anisotropic material property model	71
Figure 5.3 Progressive von mises stress profile of anisotropic material at different time steps ...	73
Figure 5.4. Pressure profile comparisons for isotropic and anisotropic microstructure	74
Figure 5.5. Early-stage stress distribution comparison between anisotropic and isotropic materials	75
Figure 5.6. Stress distribution comparison between isotropic materials	75
Figure 5.7. Particle level comparison of stress-time profile between anisotropic and isotropic materials	76
Figure 5.8. Stress particle wave velocity-time profile comparisons for anisotropic and isotropic materials	77
Figure 5.9. Maximum pressure vs time comparison for isotropic and anisotropic microstructure	78
Figure 5.10. Maximum shear stress vs time comparison for isotropic and anisotropic microstructure	78

ABSTRACT

Accurate predictions of the behavior of energetic materials necessitates incorporation of all possible variables affecting the mechanical behavior of such materials into numerical models. This work presents findings in the combined experimental and computational study of the effects of anisotropy and microstructure on the behavior of HMX-based energetic materials. Large single crystal samples of β -HMX were meticulously created by solvent evaporation for experimental purposes, and respective orientations were identified via x-ray diffraction. Indentation modulus and hardness values were obtained for different orientations of β -HMX via nanoindentation experiments. Small-scale dynamic impact experiments were performed, and a viscoplastic power law model fit, to describe the anisotropic viscoplastic properties of the crystal. The anisotropic fracture toughness and surface energy of β -HMX were calculated by studying indentation-nucleated crack system formations and fitting the corresponding data to two different models, developed by Lawn and Laugier. It was found that the $\{011\}$ and $\{110\}$ planes had the highest and lowest fracture toughnesses, respectively. Drop hammer impact tests were performed to investigate effects of morphology on the impact-induced thermal response of HMX. Finally, the anisotropic properties obtained in this work were applied in a cohesive finite element simulation involving the impact of a sample of PBX containing HMX crystals with varying orientations. This showed temperature spikes to occur where the crystals are in closer proximity. Cohesive finite element models were generated of separate microstructure containing anisotropic or isotropic properties of HMX particle. In comparison, the isotropic model had more even distributions of stress through the material as expected, however, the anisotropic model withstood larger amounts of stress for longer than the isotropic model.

1. INTRODUCTION

Understanding the behavior of energetic materials (EMs) is becoming increasingly important as they are relied on for more functions in the industry. There are currently various applications of energetic materials in the defense, aerospace and civil industries which necessitates study into their behavior when exposed to various environments. A typical EM mixture consists of about 60% to 95% solid oxidizer material and the rest is comprised of a polymeric binder (David J Benson & Paul Conley, 1999). Put together, this mixture is commonly known as a polymer bonded explosive (PBX). Energetic mixtures exhibit distinctly different thermal, mechanical, and chemical behavior than pure materials because their microstructure introduces internal boundary effects at the mesoscale (Baer, 2002). Due to their complex microstructure, energetic materials are known to be sensitive to mechanical and thermal stimuli, which may lead to a sudden localized temperature rise, called hot spots, in areas of the microstructure. Hot spots provide a means for unintentional or uncontrolled detonation when they occur in energetic materials. This necessitates study into the underlying physical processes associated with their initiation and the materials with which they are associated.

This work focuses on the oxidizer, Cyclotetramethylene Tetranitramine, also known as HMX and its respective mixtures, HMX-based PBXs. As a high explosive energetic material, HMX is used by the military, in the aerospace industry as a component of rocket propellants, and in the civil industry as an explosive charge. For an energetic material such as HMX, the sensitivity of the material to shock, the possibility of initiation, and the subsequent reaction is known to be controlled by processes occurring at the crystal level (Baer, 2002). It would therefore follow that physical characteristics such as the crystal's morphology, purity, and internal and external defects

would play vital role in sensitivity of the energetic material (Sivabalan et al., 2007). In the same line, previous experiments point to the anisotropic nature of β -HMX, the most thermodynamically stable polymorph of HMX being critical in determining the performance of HMX based polymer bonded explosives (Baer, 2002). In order to fully characterize the mechanical behavior and related stability of an energetic material, a good understanding of the defect structure is important (Gallagher, Sherwood, & Vrcelj, 2014).

When it comes to external effects, the formation of the hot spots can be determined by the physical properties of the explosive crystal or particle. In its natural form, β -HMX exhibits a myriad of shapes and a slight variation of crystal shape leads to different initiation characteristics. It has been shown that one of the ways to lower the sensitivity of an EM towards mechanical stimuli is to control the crystal size and morphology to cubic or spherical shape (Sivabalan et al., 2007). Therefore, smoothing of material boundaries is known to reduce the shock sensitivity of the explosive.

1.1 Objectives

The main objective of this work is to study the effects of microstructure on the thermomechanical response of HMX based energetic materials. This is accomplished through multiple sub-objectives which are covered in chapters. They are divided into experimental efforts to investigate the anisotropic and morphological properties affecting the mechanical response and failure characteristics of single crystal HMX, detailed in chapters 2, 3, and 4, and numerical efforts to incorporate microstructural effects into the simulation of HMX based PBX material behavior, detailed in chapter 5.

Chapter 2 details the methods and results of experimentally measured anisotropic constitutive parameters of β -HMX. This is achieved via external loading applied to and along specific planes of β -HMX crystals. Modulus parameters are obtained for each plane via nanoindentation experiments on prepared samples. Viscoplastic constitutive parameters are obtained for each plane by fitting the load related values obtained from small-scale dynamic impact experiments to a power law model.

Chapter 3 details methods and resultant values of experimentally measured anisotropic fracture properties of β -HMX. Anisotropic fracture toughness and surface energy values are obtained for β -HMX via indentation induced crack measurement. The measured values are fitted to two proposed literature models and compared. The resultant values of fracture toughness and surface energy are presented for the (010), {110}, and {011} planes of β -HMX.

Chapter 4 details the experimental observation and characterization of the morphological effects of single crystal HMX on local temperature rise (hotspot initiation) and intensity. In, this work, ignition-level impact on HMX crystals embedded in a polymeric binder is achieved through the drop hammer test. Simultaneously high spatially and temporally resolved measurement of local temperature rise obtained by a combination of two thermal cameras. Spatial resolution microscale images of the impact are obtained via a mid-wavelength infrared (MWIR) camera while temporally resolved microsecond measurements of local temperature rise obtained by a 1-D linear array camera.

Chapter 5 presents results for simulations performed with anisotropic material properties obtained in previous chapters. Simulations are performed for two types of digital generated microstructure, having anisotropic and isotropic material properties, respectively. The simulations

are compared to study the potential quantitative and qualitative effects of incorporating anisotropy into HMX-based PBX simulations.

2. EXPERIMENTAL MEASUREMENTS OF ANISOTROPIC CONSTITUTIVE BEHAVIOR OF β -HMX CRYSTALS

Ayotomi Olokun¹ (aolokun@purdue.edu), Abhijeet Dhiman¹ (adhiman@purdue.edu), *Vikas Tomar¹

¹School of Aeronautics and Astronautics, Purdue University

701 W. Stadium Ave, IN, 47907, USA

*Corresponding author, **Phone:** (765)-494-3423 **Email:** tomar@purdue.edu

Abstract

For energetic crystals such as HMX, the sensitivity of the material to shock, the possibility of initiation, and the subsequent reaction is known to be controlled by processes occurring at the crystal level. The anisotropic nature of β -HMX can be critical in determining the performance of HMX based polymer bonded explosives (PBX), which are widely used across multiple industries as propellant or explosives. In this work, we experimentally obtain constitutive parameters for characterizing the response of multiple planes of β -HMX crystals to external loading. Nanoindentation and small-scale dynamic impact experiments were performed on multiple planes of β -HMX crystals to study anisotropic material behavior and measure constitutive elastic and non-elastic parameters. Findings regarding material properties for the (100), (010), (001), {110}, and {011} planes of β -HMX are presented and compared with literature data.

Keywords: HMX, Energetic Materials, Anisotropy, Nanoindentation, Hardness

2.1 Introduction

Accurate characterization and prediction of the mechanical behavior of energetic materials (EMs) requires in-depth understanding of their physical properties and of their response to external stimuli. There are many material responses whereby it is important to understand non-initiating behaviors, including deformation and failure, as damage may alter the safety parameters of these explosive material and set a new initial condition for future performance (Hooks, Ramos, Bolme, & Cawkwell, 2015). For an energetic material such as HMX, sensitivity to shock, the possibility of initiation, and the subsequent reaction is known to be controlled by processes occurring at the crystal level. HMX occurs in four polymorphic forms, α , β , δ and ϵ . Of these, the most thermodynamically stable phase is β -HMX (Gallagher et al., 2014). Thermal stability of the β -HMX crystalline phase makes it a good candidate to characterize effect of anisotropy on HMX material behavior. Previous experiments have pointed to the anisotropic nature of β -HMX being critical in determining the performance of HMX based polymer bonded explosives (PBX) (Baer, 2002). The main failure mechanisms in energetic materials have been identified as particle fracture, interfacial failure between particle and binder, and interfacial failure between particles (S.J.P, J.E., & J.M., 1993). With respect to particle fracture, due to the anisotropic nature of HMX, it is known that deformation in single crystals of β -HMX is orientation dependent and fracture tends to occur along cleavage planes. For instance, indentation experiments performed by Palmer and Field (Palmer & Field, 1982) on cleaved crystals determined the cleavage in β -HMX to take place along the $\{011\}$ crystallographic planes.

The ability to understand and, in turn, accurately predict the behavior of energetic materials critically relies, in part, on understanding the elasticity of the material, as the structure and compressibility of the material are relevant regardless of initiation shock mechanics (Hooks et al.,

2015). Description of the anisotropic elastic behavior of β -HMX has been widely investigated, however, a significant portion of the description of this behavior is obtained via molecular dynamics related numerical methods (Sewell, Menikoff, Bedrov, & Smith, 2003). Experimentally, it has proven difficult to measure elastic properties of energetic crystals such as β -HMX due to their anisotropic nature requiring complex geometric considerations and their brittle nature yielding relatively minute strains before failure (Rae, Hooks, & Liu, 2006). Previous experimental methods involving elastic constant determination for β -HMX have involved the use of techniques such as impulsive stimulated light scattering (ISLS) (Zaug, 1998), impulsive stimulated thermal scattering (ISTS) (Sun, Winey, Gupta, & Hooks, 2009) and Brillouin scattering (Stevens & Eckhardt, 2005). However, these methods, when compared, produce a variance in values that is yet to be fully understood or explained (Hooks et al.). Nanoindentation as an experimental procedure has also been used in attempts to characterize the hardness and modulus of β -HMX in previous studies (Burch, Yeager, & Bahr, 2017; Kucheyev, Gash, & Lorenz, 2014; Li, Tan, Kang, Xu, & Tang, 2010; Palmer & Field, 1982). The results from these studies also provide unexplained variance which may only be fully understood with more work in the area.

With respect to energetic materials, hot spots are regions in the microstructure whereas the initiated volume is sufficiently large, and temperature is sufficiently high to start the chemical reactions leading to detonation. Friction, or interfacial interaction between particles as mentioned above, among other mechanisms, is known to be a cause of hot spot initiation. Susceptibility of an energetic material to this form of failure, most adequately described by the frictional sensitivity of the material, has been shown to be dependent on multiple factors, of which hardness has been speculated to be the most important (Harris, United, & National Technical Information, 1982). In

addition to elastic properties, this work also presents a study of the anisotropic material hardness and viscoplasticity of β -HMX.

Currently, with few exceptions, simulation of the mechanical behavior of HMX-based energetic materials in the mesoscale generally overlooks the anisotropic properties of the material, however the argument can be made that incorporation of anisotropic properties of HMX crystals may improve the current ability to predict the behavior of these materials. Examples of the aforementioned exceptions can be seen in work done by Wang et al. (X. Wang, Wu, & Huang, 2017), in which a full field method was employed to model the local damage behavior of a HMX-based EM, using an elasto-viscoplastic model for the HMX crystals and a viscoelastic model for the binder and interface. Other works simulate the anisotropic material behavior HMX to determine anisotropic material responses, work by Conroy et al. (Conroy, Oleynik, Zybin, & White, 2008) modeled the behavior of β -HMX crystals using first principles density functional theory (DFT) to study the anisotropic behavior of principal stresses measured in different planes of HMX single crystal. They found that the anisotropic model predicted experimental results that adequately matched existing data. Zamiri et al. (Zamiri & De, 2011) also worked on numerically predicting the anisotropic plastic response of modeled single crystals of HMX based on experimental data. This work focuses on experimentally characterizing anisotropic quasistatic as well as dynamic local constitutive material properties of β -HMX crystals using indentation based static and dynamic schemes.

2.2 Methods

This section covers brief explanation of the experimental methods and theories to be used in this work. These methods have been covered in detail in previous works (A. Olokun, Prakash,

Emre Gunduz, & Tomar, 2019; Prakash, Emre Gunduz, & Tomar, 2018; Prakash, Gunduz, Oskay, & Tomar, 2018; H. Wang et al., 2019).

2.2.1 Sample Preparation

Untwinned single crystals of β -HMX were formed by controlled solvent evaporation, at room temperature, from a saturated solution of raw HMX in HPLC grade 99.8% pure acetone. The solution was mixed at ratio of 0.024:1 by weight of HMX to acetone respectively and measured into vials with perforated caps for slow evaporation. The descriptions here are of monoclinic single crystal β -HMX in space group $P2_1/n$. with lattice parameters $a = 0.654$ nm, $b = 0.736$ nm, $c = 1.104$ nm, and $B = 102.66^\circ$. Two main morphologies of single crystal were observed, and the respective orientations were identified through x-ray diffraction shown in Figure 1 below.

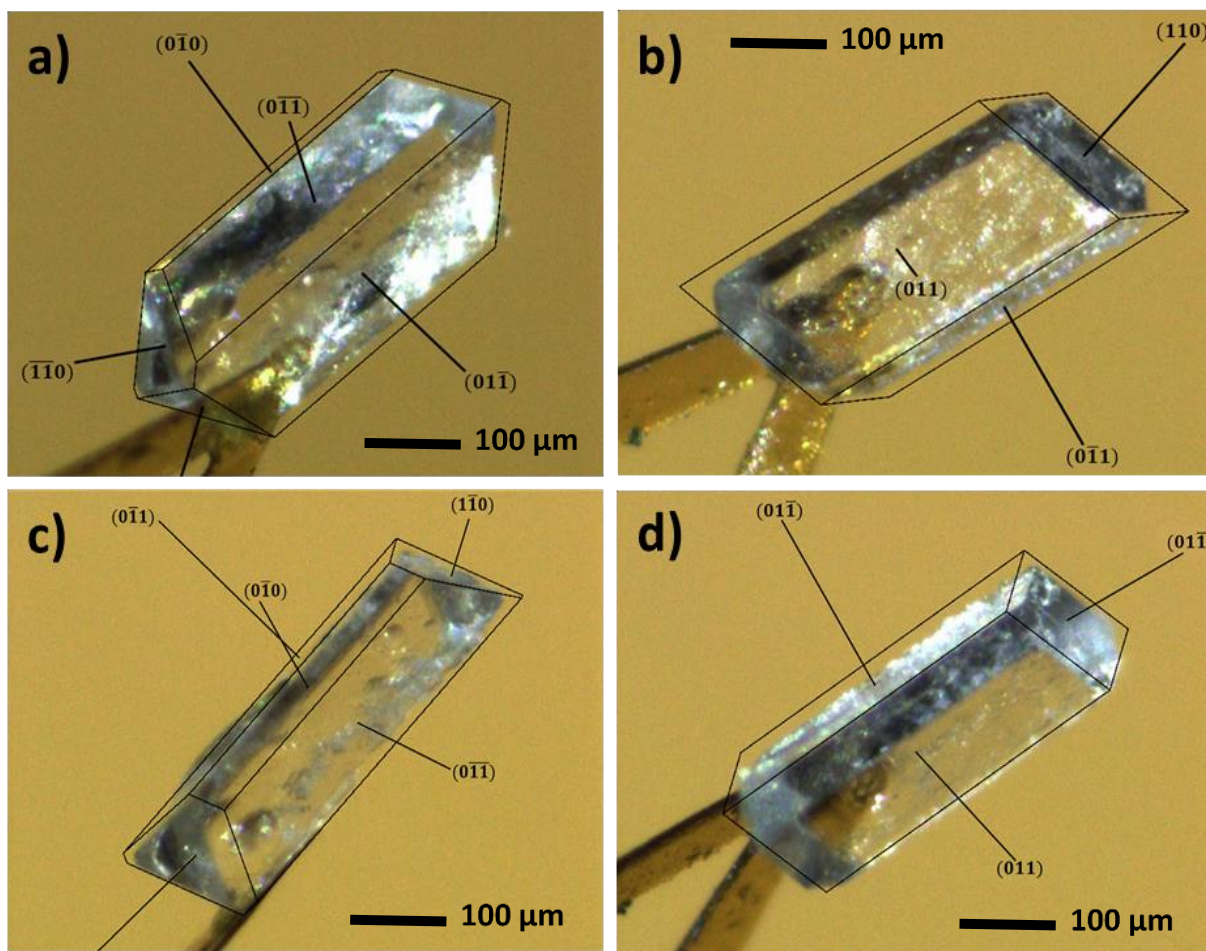


Figure 2.1. Identified faces of β -HMX crystals for two morphologies: a) and c) show morphology 1 and b) and d) show morphology 2.

The first morphology observed, denoted ‘morphology 1’, exposed facets corresponding to the (010) , $\{011\}$, and $\{110\}$ crystallographic planes, while the second morphology displayed exposed facets corresponding to $\{011\}$ and $\{110\}$ planes only. In both morphologies, the facets corresponding to the $\{011\}$ planes appeared to be of preferred growth, displaying larger surface areas in most crystals observed. The morphologies observed also grew longitudinally along the ‘a’ crystallographic axis as shown in Figure 2. The length distribution (along the preferred a-crystallographic axis) of fully formed crystals varied from 200 μm to 4 mm with an average length of 2 mm and width (approximately perpendicular to the a-axis) of 1 mm. Typically crystals equal

to or larger than 1mm were chosen for experiment purposes to provide sufficient surface area for multiple indentations.

Experiments for further characterization of elastic behavior required access to indentation axes perpendicular to planes that were not exposed in the single crystal morphologies that presented, such as the (100) and (001) planes corresponding to the a and c crystallographic axes. In such cases, crystals were embedded in a hardened epoxy and cleaved to expose the necessary planes and sanded down with decreasing particle sizes. In particular, the hardened epoxy used here was the ‘Aluminite Amazing Casting Resin’ due to its lower volumetric contraction on curing. The surfaces were then polished using silicon carbide sandpaper with a $<8\mu\text{m}$ average particle diameter.

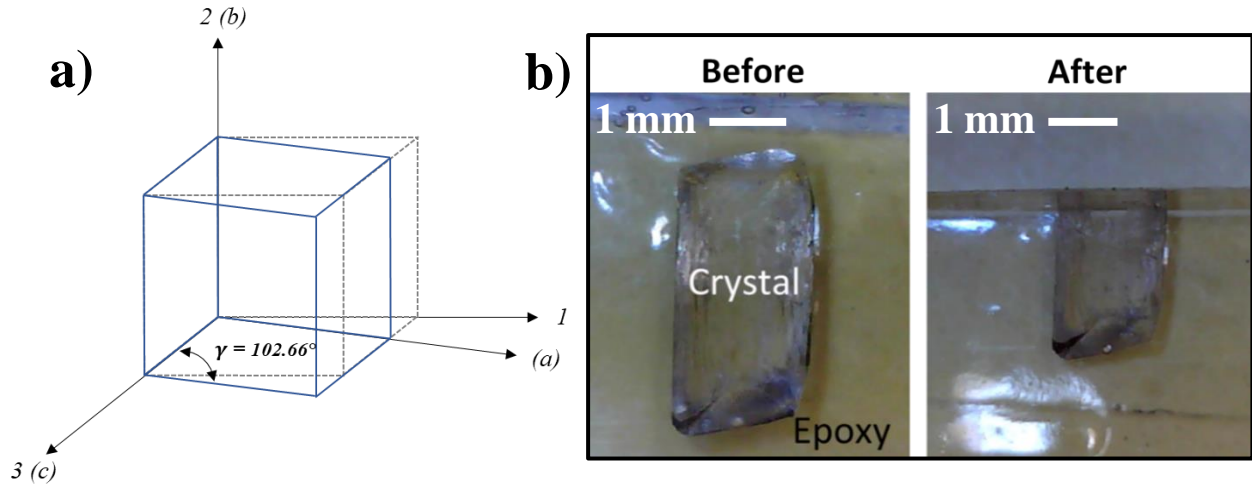


Figure 2.2. (a) Crystallographic axes and planes of monoclinic β -HMX (b) Before and after images showing cleaving of embedded β -HMX crystal to expose (100) plane

2.2.2 Anisotropic Elastic Constitutive Properties

This work presents experimentally obtained indentation material properties to describe the anisotropic elastic behavior of β -HMX as a response to external loading applied to different planes of the crystal. This section describes the experimental and theoretical methods employed.

2.2.2.1 Nanoindentation

Nanoindentation has been used in multiple studies of material elastic behavior and has proven to be a reliable technique to measure local elastic material properties (Marsh, Han, Verma, & Tomar, 2015; H. Wang et al., 2019; H. Wang, Thomas, Okuniewski, & Tomar, 2020; Zhang et al., 2017), extending to elastic properties of energetic materials (Palmer & Field, 1982). Properties such as elastic modulus and hardness can be easily obtained via nanoindentation due to the underlying fact that displacements recovered during unloading are known to be mainly elastic. In this work, a NanoTest platform (Micro Materials Ltd., UK) (Verma & Tomar, 2014) is used to perform the indentation experiments. Multiple indentations were performed, at various indentation depths, on each plane at room temperature with a Berkovich type indenter having a diamond tip radius of 20 nm. Figure 2a shows the indentation test setup. Sample crystals were oriented with the loading plane of interest perpendicular to the indenter and indentations were spaced with a minimum of 100 μm between each indent to limit the possibility of coalescence between indents. The machine compliance is corrected as detailed in previous work (H. Wang et al., 2019).

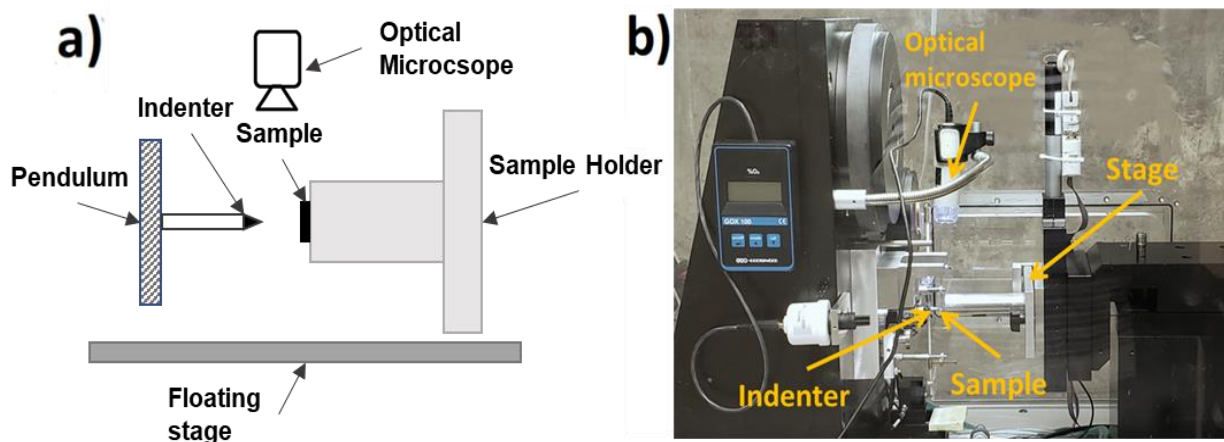


Figure 2.3. Nanoindentation experiment setup

2.2.2.2 Hardness and Modulus Evaluation

Each indentation experiment is represented by data points on a load-depth plot, an example of which can be observed in Figure 1b. The Oliver–Pharr’s method (Oliver & Pharr, 1992) is used to calculate the indentation modulus and hardness. In the case of isotropic materials, the Oliver-Pharr method has been shown to estimate material properties such as Young’s modulus to a high accuracy, about 4% of literature values. However, this is not the case for anisotropic materials as the indentation modulus represents more of a weighted average value as deformation involves multiple directions (Fan, Swadener, Rho, Roy, & Pharr, 2002). Therefore, in this work, the indentation moduli for each direction will be obtained individually, as weighted averages, and compared to actual elastic constants for those directions. To obtain the necessary parameters, the values obtained from the indentation experiment are fit the load-depth curve obtained from the experiment.

$$P = A_m(h - h_f)^m \quad (1)$$

where A_m and m are parameters obtained empirically from the power law equation, h is the indentation depth corresponding to a specific load P , and h_f is the plastic indentation depth remaining after the load has been completely removed. The indentation hardness can be calculated as,

$$H = \frac{P_{max}}{A} \quad (2)$$

For a Berkovich indenter, the contact area can be estimated as $24.5h_c^2$, where h_c is the contact depth. The reduced indentation modulus (M_r) is calculated as,

$$M_r = \frac{\sqrt{\pi}}{2} \frac{S}{\sqrt{A}} \quad (3)$$

The indentation modulus of the material is then obtained from the relation,

$$\frac{1}{M_r} = \frac{1 - \nu^2}{M} + \frac{1 - \nu_i^2}{M_i} \quad (4)$$

Constants ν and M are the Poisson's ratio and indentation modulus of the sample, while ν_i and E_i represents Poisson's ratio and Young's modulus of the indenter, respectively. The Poisson ratios used in this work were obtained from values presented in literature (Sewell et al., 2003) and approximated thus,

$$\nu_i = \frac{\nu_{ij} + \nu_{ik}}{2} \quad (5)$$

Therefore, 0.33, 0.3, and 0.4 were used for ν_1 , ν_2 , ν_3 and respectively.

2.2.2.3 Indentation Size Effect (ISE)

Previous studies of hardness obtained by nanoindentation have shown a dependence of the measured values of hardness on ‘indentation size’, i.e. the indirect variation of hardness with indentation depth. This phenomenon is referred to as the indentation size effect (ISE) and some possible explanations of the causes of this behavior, particularly in crystalline materials, have been proposed in literature (Nix & Gao, 1998), for instance the strain gradient plasticity theory (H. Wang et al., 2019). The hardness eventually reaches a constant value which can be quantified according to the Nix-Gao relation (Nix & Gao, 1998) as:

$$\frac{H}{H_0} = \sqrt{1 + \frac{h^*}{h}} \quad (6)$$

Here, H is the hardness value corresponding to a certain indentation depth h . H_0 is the final constant hardness value at infinite depth, and h^* is a characteristic length parameter, both of which are important parameters necessary for the definition of constitutive equations in strain gradient plasticity theory (H. Wang et al., 2019). Equation 6 can be rewritten as,

$$H^2 = H_0^2 \left(1 + \frac{h^*}{h} \right) \quad (7)$$

H and h values are obtained here from experiment results.

2.2.3 Anisotropic Strain-Rate-Dependent Viscoplastic Constitutive Model

In order to describe the anisotropic viscoplastic behavior of β -HMX crystals, a viscoplastic constitutive power law is defined, and experimental orientation-dependent viscoplastic parameters are obtained in this work. In a previous work (A. M. Olokun, Prakash, Emre Gunduz, & Tomar, 2020), the behavior of Hydroxy-Terminated Polybutadiene (HTPB)-HMX based PBXs have been modeled using Cohesive Finite Element Method (CFEM) based simulation software. The developed CFEM model used polycrystalline HMX parameters in order to obtain an approximated description of the viscoplastic behavior of the material. Here, we present a study into the orientation dependence of these parameters, giving a more detailed description of the range of possible behavioral limits and how well previous approximations fit into this range.

2.2.3.1 Dynamic Small-Scale Impact Experiments

The viscoplastic constitutive parameters are obtained via nanoscale dynamic impact in regions of interest on selected β -HMX crystal phases. The specific equipment used for this experiment is impact module of Micro Materials, UK. This equipment and the corresponding

technique have been used to successfully obtain mechanical properties of other energetic materials at small scale such as HTPB-AP interface (Prakash, Olokun, Emre Gunduz, & Tomar, 2019). In this experimental setup, the sample is positioned in front of a spherical impactor with the plane face of interest oriented perpendicular to the impactor. The sample is mounted on a three-dimensional stage and the entire setup sits on a “floating” platform; thus, the sample can be moved freely in all directions. The impactor is a conical indenter of radius $1\text{ }\mu\text{m}$, it is mounted on a vertical pendulum which hangs on a frictionless spring. Impact on the sample is achieved through the use of electromagnets on the vertical pendulum and as such different magnitudes of desired impact force can be achieved. The schematic for the equipment setup is shown in Figure 4 below.

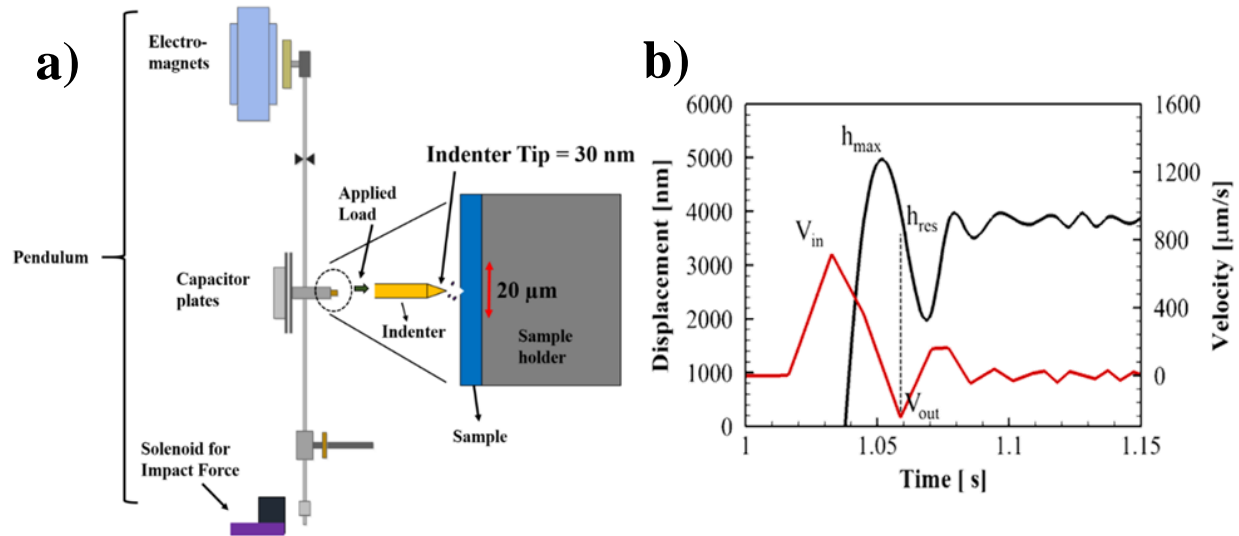


Figure 2.4. (a) Small-scale dynamic impact experiment setup (b) Load-depth plot and derived velocity-time plot from one impact experiment

Depth is measured by the distance between the capacitors located behind the impactor and the velocity is obtained by a continuous differentiation of the depth-time plot. Impact is performed on each plane of interest on multiple samples. The stress, strain, and average strain rate of the

experiment can be obtained using values from the depth-time and velocity-time plot. Figure 4b shows an example of a plot output from one impact experiment. The strain rate is calculated as,

$$\dot{\varepsilon} \approx \frac{V_{in}}{h_{max}} \quad (8)$$

where h_{max} is the maximum depth and V_{in} is the maximum velocity. The strain and stress are also calculated as,

$$\varepsilon \approx \frac{h_{res}^2}{h_{max}^2} \quad (9)$$

$$\sigma \approx \frac{P}{\pi h_{max}^2} \quad (10)$$

where h_{res} is the residual depth and P is the impact load. These values are fit to a power law model which is assumed to represent the effective stress-effective viscoplastic strain relationship.

2.2.3.2 Viscoplastic Constitutive Parameter Evaluation

Following the method outlined by Prakash et al. (Prakash, Emre Gunduz, et al., 2018), we obtain the orientation dependent viscoplastic model parameters for each plane by fitting the load related values obtained above to a power law model:

$$\bar{\sigma} = A(\bar{\varepsilon}^{vp})^n, \quad (11)$$

Where:

$$A = F_0 \left(\frac{\dot{\bar{\varepsilon}}^{vp}}{\dot{\bar{\varepsilon}}^0} \right)^m. \quad (12)$$

Here, $\bar{\varepsilon}^{vp}$ is the effective viscoplastic strain, and $\dot{\bar{\varepsilon}}^{vp}$ is the effective viscoplastic strain rate. The coefficient, A , is plotted against the effective viscoplastic strain rate on a log-log scale to obtain χ_0 and m parameters more simply as the slope and intercept of the plot. The parameters fit to a

power law model useful for predicting the constitutive behavior of the material at higher strain rates (Prakash, Olokun, Emre Gunduz, et al., 2019). The validity of the viscoplastic equivalent stress-strain power law for modeling the behavior of this material has been evaluated in previous work (Prakash, Emre Gunduz, et al., 2018). Here, we obtain the parameters to define the anisotropic viscoplastic behavior in each different orientation of interest in the examined single crystal.

2.3 Results and Discussion

Using the process detailed above, at different loads, multiple indentations were performed on each plane of interest on the HMX crystals. Grown crystal samples presented smooth surfaces parallel to (010), {011}, and {110} planes and these were used in experiments without modification. Indentations were also performed on planes perpendicular to the three crystallographic axes to characterize behavior on these planes. Two out of three of these planes, (100) and (001) perpendicular to the monoclinic a and c axes, respectively, did not present parallel facets naturally in the samples grown. As such, modifications, detailed above (Figure 2), were made to expose them. The plane perpendicular to the b crystallographic axis, the (010) plane, naturally presented on our crystal samples as shown in Figure 1.

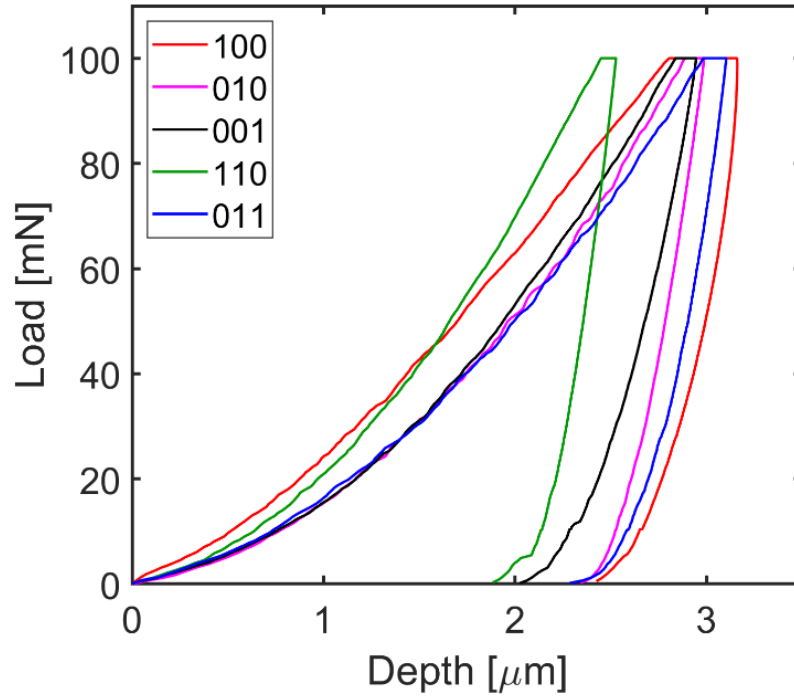


Figure 2.5. Indentation load vs depth plot comparisons of different planes of β -HMX crystal

In order to define the indentation moduli for the three main axial directions, an additional plane was required to be exposed for loading. Indentation moduli corresponding to the elastic moduli, E_{22} and E_{33} , were obtained directly as the b and c crystallographic axes were intentionally oriented along the 2 and 3 axes as shown in Figure 2a. The indentation modulus corresponding to the directional elastic modulus, E_{11} , however, were obtained by loading along a direction determined by the cross product between the a and c crystallographic axes. The results of the moduli obtained by indentation for these three directions are presented in Table 1.

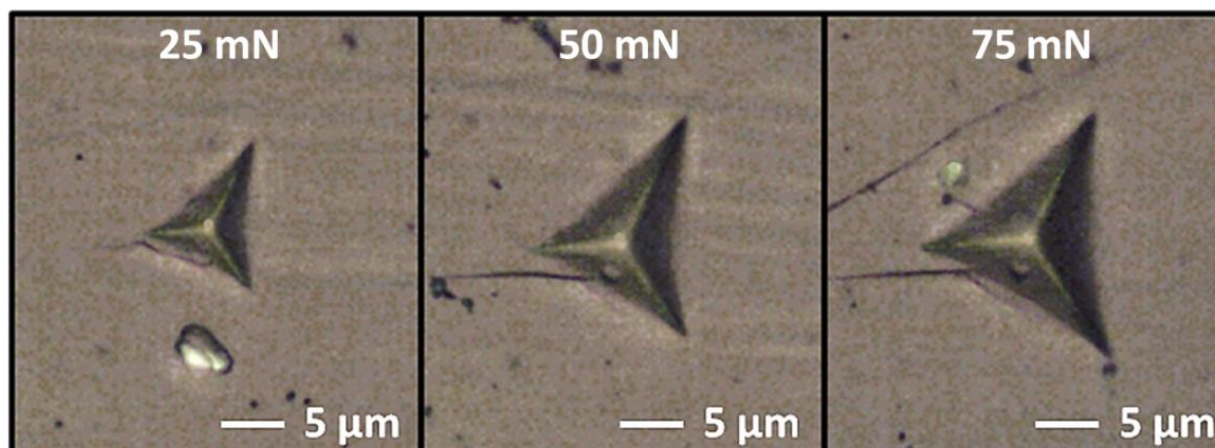


Figure 2.6. Imaged indentations performed on the (010) facet of a β -HMX crystal.

Table 2.1. Indentation moduli obtained from this work in comparison to elastic moduli presented in published works.

E_{ii}	This work	Li et al. (Li et al., 2010)	Kucheyev et al. (Kucheyev et al., 2014)	Stevens et al. (Stevens & Eckhardt, 2005)	Zaug et al. (Zaug, 1998)	Sewell et al. (Sewell et al., 2003)
E_{11}	14.21	--	--	8.58	11.82	14.23
E_{22}	16.65	23.18	17.6	10.95	24.04	14.88
E_{33}	11.65	26.05	--	5.37	9.69	12.85

Our results for modulus in the E_{22} direction showed good agreement with the value presented by Kucheyev et al. (Kucheyev et al., 2014), in which Berkovich indentations were performed. The work of Li et al. (Li et al., 2010) also presents moduli for different facets of β -HMX crystals as obtained by Berkovich indentation, however our values are significantly lower than their presented results. As discussed above, this is not unique to nanoindentation as other means of experimental determination of elastic moduli for this material also present discrepancies. It should be noted however, that values obtained present a similarity to values obtained by molecular dynamics simulations (Pereverzev & Sewell, 2020) with a maximum of 12% error, and otherwise reasonably fit into the statistically determined range of values presented, obtained from

both numerical and experimental methods. Moreover, the values obtained in this work agree with most works which show E_{22} to be the largest and E_{33} to be the smallest moduli.

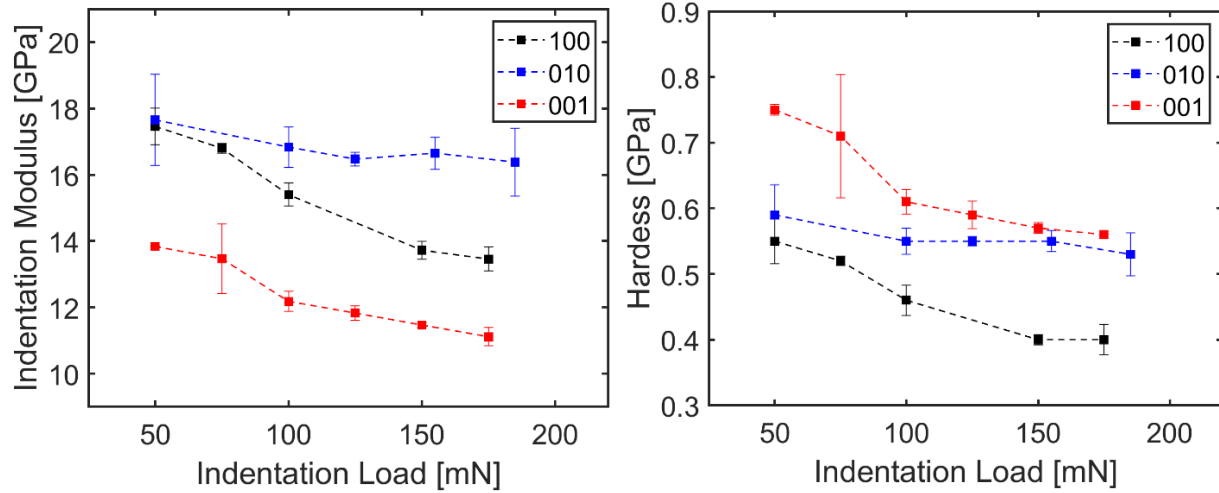


Figure 2.7. Anisotropic behavior of β -HMX crystal planes with respect to modulus and hardness

The anisotropic behavior of three different orientations with respect to indentation modulus and hardness can be observed in Figure 7. Here, the properties of planes corresponding to the three main crystallographic axes are compared and anisotropic behavior can clearly be observed in the values of measured properties with changing indentation load/depth. The hardness and plastic depth values were fit using the Nix-Gao relation detailed above, the results are shown in Figure 8. The indentation moduli, hardness, and Nix-Gao relation fitted values obtained for each plane are presented in Table 2. Li et al. (Li et al., 2010) presented hardness values for the (010) face of β -HMX as 1.13 GPa, also obtained via Berkovich indentations on the crystal facet. This is in general agreement with the value of 1 GPa, for arbitrarily oriented HMX crystals, presented by Burch et al. (Burch et al., 2017), however our value of 0.55 GPa for the same facet (010) are significantly lower and closer to the value of 0.65 GPa presented by Kucheyev et al. (Kucheyev et al., 2014).

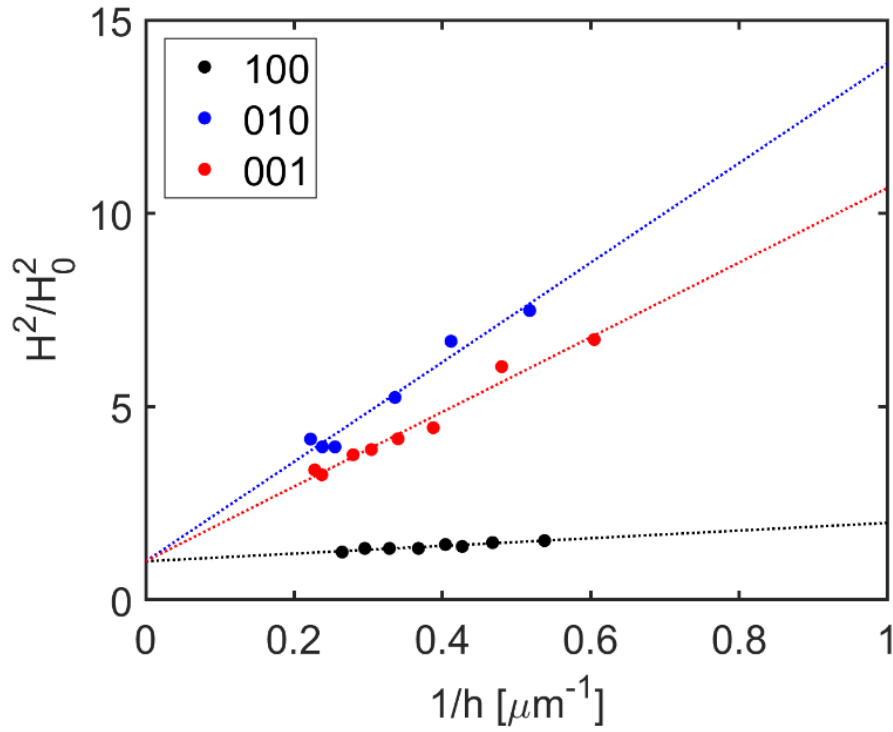


Figure 2.8. Comparisons of Nix Gao fitting of hardness data for 3 planes

A significant amount of the data on hardness for β -HMX presented in literature focuses on the Vickers Hardness Number (VHN). Studies have shown the hardness values from Vickers indentations to be similar to, however slightly lower than, values obtained for Berkovich indentations (Leitner, Maier-Kiener, & Kiener, 2017; Sakharova, Fernandes, Antunes, & Oliveira, 2009). The hardness values obtained here are higher but close in value to the VHNs; 0.41 GPa obtained by Amuzu et al. (Amuzu, Briscoe, & Chaudhri, 1976) and 0.4 GPa obtained by Palmer and Field (Palmer & Field, 1982). However, both works did not indicate specific orientations for the values. A VHN range of 0.3 – 0.36 GPa, presented by Gallagher et al. (Gallagher et al., 2014) for indentations made on the (010), {011}, and {110} planes, fall lower comparatively.

Table 2.2. Properties obtained for each tested plane of β -HMX by indentation

Plane	M [GPa]	H [GPa]	H ₀ [GPa]	h* [μ m]
100	14.84 ± 0.33	0.42 ± 0.02	0.20	12.88
010	16.65 ± 0.57	0.55 ± 0.02	0.48	0.99
001	11.65 ± 0.22	0.56 ± 0.01	0.29	9.66
110	21.04 ± 0.59	0.65 ± 0.02	0.56	127.55
011	14.79 ± 0.38	0.51 ± 0.01	0.26	8.97

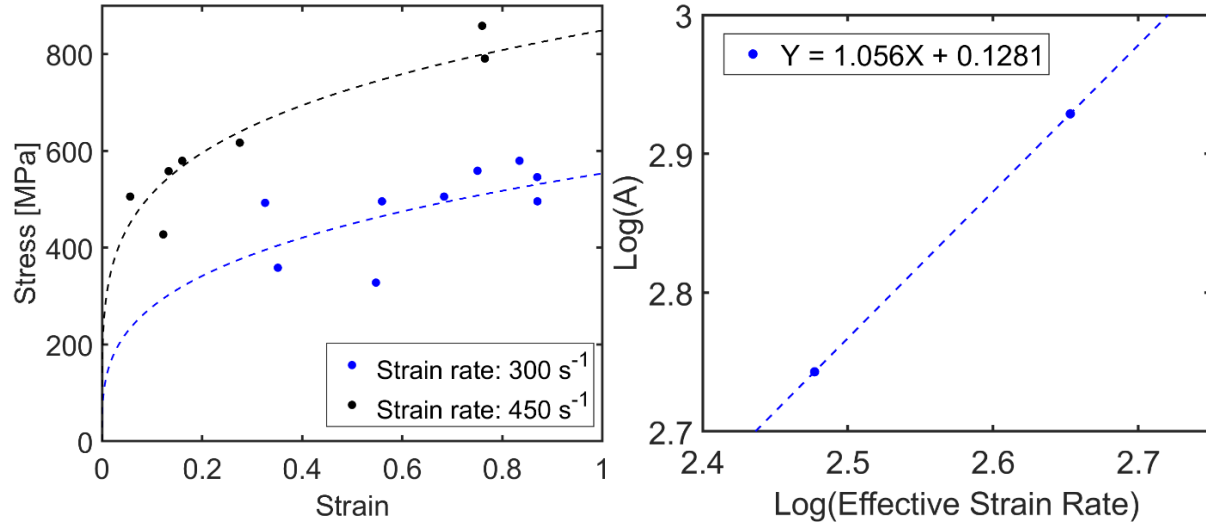


Figure 2.9. Viscoplastic model parameters are obtained by fitting impact data to viscoplastic power law from 100 plane

Viscoplastic parameters were also obtained in this work for the viscoplastic effective stress-strain power law described above. These parameters were obtained via small-scale dynamic impact experiments, to describe the viscoplastic behavior of the material. Viscoplastic parameters were obtained in previous work for polycrystalline HMX embedded in a polymeric binder (Prakash, Olokun, Gunduz, & Tomar, 2019). As the material was polycrystalline, due to the underlying

assumption of isotropy, the parameters obtained were independent of orientation. The parameters for Ammonium Perchlorate (AP) were also obtained in a previous work and both parameters are included below for comparison. The orientation dependent viscoplastic parameters for the viscoplastic effective stress-strain power law are presented in Table 3. Figure 9 shows the fitting of the data obtained for the (100) plane to the viscoplastic power law at multiple strain rates.

Table 2.3. Anisotropic viscoplastic parameters

Plane	F_0	m	n
100	1.06	0.13	0.26
010	0.46	1.17	0.33
001	0.32	1.8	0.16
110	0.11	2.1	0.59
011	0.21	1.83	0.27
AP*	0.016	1.61	0.17
Polycrystal**	0.95	0.5	0.63

*(Prakash, Emre Gunduz, et al., 2018) **(Prakash, Olokun, Gunduz, et al., 2019)

From the results presented above, we observed that viscoplastic strain for the {110} plane appears to have the highest comparative dependency on strain rate, as determined by the strain rate exponent 'm', and are predicted to have the highest values in comparison to other planes at a given strain rate and stress. This behavior is as expected as this plane has a high value of the strain hardening exponent 'n' as well. These findings appear to agree with results obtained by Zamiri et al. (Zamiri & De) in the anisotropic simulation of β -HMX, where simulation, and compared

experimental data (Rae et al.), showed the $\{110\}$ plane to be relatively more prone to plastic deformation. In addition, the results potentially corroborate work by Conroy et al. (Conroy et al.) which found maximum principal stress to be greatest for the $\{110\}$ and $\{011\}$ plane compressions. The (100) plane appears to have the lowest dependency on strain rate and resultingly low comparative viscoplastic strains. Viscoplastic behavior of AP will be closer to the behavior predicted for most planes in terms of strain rate dependency, as the strain rate exponent value is closer to the average. However, in comparison to most planes, the values for polycrystalline HMX predict low viscoplastic strains closer to the lowest values of the (100) plane, with similar exponent values. Figure 10 shows the comparative values of the exponent parameters.

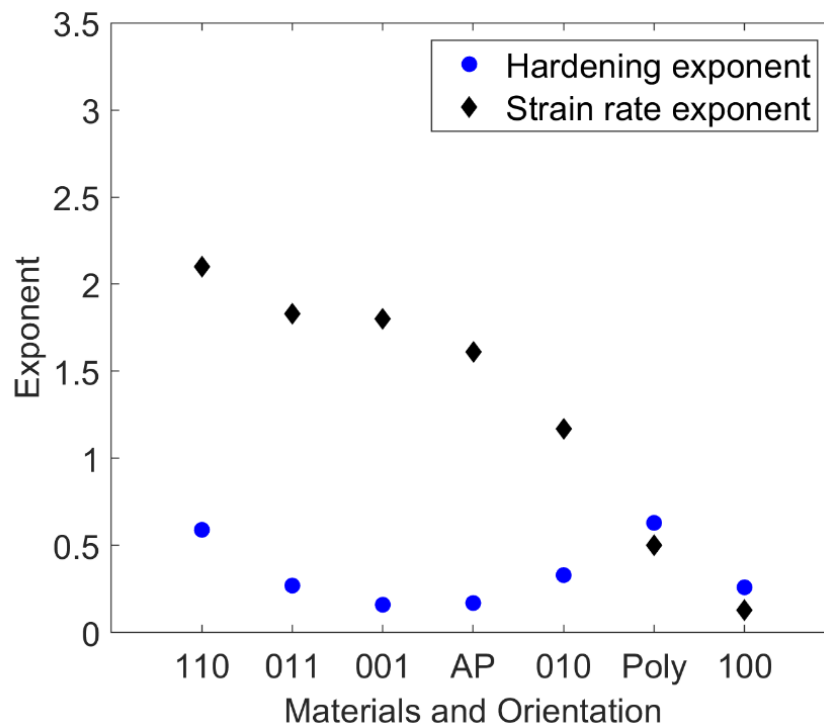


Figure 2.10. Comparisons of exponent values in viscoplastic model

An interesting finding is that the planes with the most and least comparative viscoplastic strains also had the highest and lowest hardness, respectively. This result is considered to be as expected as materials with higher hardness values will in turn have a higher values of yield strength.

2.4 Conclusions

In this work, experimentally obtained constitutive parameters for modeling the mechanical behavior of external loading applied to different planes of β -HMX were presented. Indentation modulus and hardness values were obtained for each plane via nanoindentation experiments. Results obtained fit reasonably into a statistically determined range of values obtained from both numerical and experimental methods presented in literature. Nanoindentation has been shown to estimate the elastic modulus of isotropic materials to a 4% accuracy and as such, these results and future validations may present a discussion on the possibility of nanoindentation providing a means of obtaining acceptable approximations of anisotropic elastic moduli.

Viscoplastic constitutive parameters were also obtained for each plane by fitting the values obtained from dynamic impact experiments to a power law model. The results showed the {110} plane to have the highest comparative viscoplastic strains respectively at a given strain rate and stress, which is supported by other findings in literature. The parameters presented in this work could provide a more accurate description of the behavior of β -HMX in the prediction of HMX based EMs.

3. EXPERIMENTAL MEASUREMENTS OF ANISOTROPIC FRACTURE PROPERTIES OF β -HMX CRYSTALS MEASURED BY NANOINDENTATION

Ayotomi Olokun¹ (aolokun@purdue.edu), Abhijeet Dhiman¹ (adhiman@purdue.edu), *Vikas Tomar¹

¹School of Aeronautics and Astronautics, Purdue University
701 W. Stadium Ave, IN, 47907, USA

*Corresponding author, **Phone:** (765)-494-3423 **Email:** tomar@purdue.edu

Manuscript under preparation.

3.1 Introduction

Understanding the initiation conditions of energetic materials (EMs) is considered an important step to accurately predicting their behavior. This largely involves studying non-initiating behaviors such as the material's intrinsic mechanical properties as well as its response to external stimuli, such as static and rate dependent loading. This is especially important as damage at production or storage stages of the material could alter the initiation conditions for future performance (Hooks et al., 2015). The mechanical behavior of these materials can be attributed to their complicated microstructure and physical processes occurring at multiple length scales (Prakash, Gunduz, et al., 2018). For an energetic material such as HMX, the sensitivity of the material to shock, the possibility of initiation, and the subsequent reaction is known to be controlled by processes occurring at the crystal level. In addition, single crystals of HMX display anisotropic material behavior and previous studies have presented results which suggest that the

anisotropic nature of β -HMX, the most thermodynamically stable polymorph of HMX, could be critical in determining the performance of HMX based polymer bonded explosives (PBX) (Baer, 2002).

In regard to studying the initiation of energetic materials, an important phenomenon is the nucleation of ‘hot spots’. Hot spots, in this context, are regions in the microstructure of EMs where the initiated size and temperature are sufficiently high to cause detonation. Some mechanisms known to initiate hot spots are adiabatic compression of trapped gas, friction between impacting surfaces, viscous heating of surrounding material, and so on. It is known that the high stress field generated at the tip of a crack as it propagates can lead to plastic deformation, however the hot spots generated at crack tips of energetic materials rarely lead to detonation single handedly. The reason for this being that the surface energy involved in the propagation is insufficient to produce both the required temperature and size to cause ignition (Field, 1992). With this in mind, it has also been shown that fracture in explosive materials leads to the production of ‘gaseous decomposition products’ which generate gas pockets in the material, further increasing the susceptibility of the material to hot spots by adiabatic compression of the trapped gas (Field, 1992).

Fracture behavior in crystals of β -HMX is known to be orientation dependent due to the anisotropic nature of the crystal. Deformation, such as slip and fracture, have been found to occur on specific planes of the crystal depending on which orientation the crystal is loaded (Dick, Hooks, Menikoff, & Martinez). Findings which are supported by multiple works including indentation experiments on cleaved β -HMX crystals experiments (Palmer & Field, 1982). Microhardness indentation has been widely used to evaluate anisotropy in material properties of single crystals (Burch et al., 2017). The use of sharp indenters in particular on brittle materials has been shown produce cracks that propagate out from the corners of the indentations. The sizes of the cracks

formed serve as a basis for the determination of the fracture toughness of the material, from which we can also obtain the surface energy, both useful properties to describe fracture behavior of a material.

Some studies have measured the fracture properties of β -HMX through indentation methods. Palmer and Field measured the fracture surface energy of the $\{011\}$ face of β -HMX crystals to be 0.4 J/m^2 by indentation (Palmer & Field, 1982), while Wang et al. (D. D. Wang et al., 2011) measured the fracture toughness of the (010) face to be approximately $0.093 \text{ MPa/m}^{1/2}$. Burch et al. also performed indentation experiments on multiple single crystals of HMX and reported the fracture toughness for the crystal to be approximately $0.28 \text{ MPa/m}^{1/2}$ (Burch et al., 2017). This work aims toward obtaining values for both fracture toughness and surface energy measured by indentation on multiple planes of the β -HMX crystal to observe the extent of anisotropy in this behavior.

3.2 Methods

3.2.1 Sample Preparation

Experiments were performed on large untwinned single crystals of β -HMX, formed by recrystallization of particulate HMX. The HMX, in powdered form, was dissolved in HPLC grade acetone in a sonic bath until saturation, and crystal growth was achieved by slow, controlled solvent evaporation at room temperature. All indentations were performed on monoclinic single crystal β -HMX in space group $P2_1 / n$, parameters of which are displayed in Figure 1. These parameters were obtained via x-ray diffraction, performed on smaller crystals ($\sim 200 \text{ }\mu\text{m}$ length) shown in Figure 2.

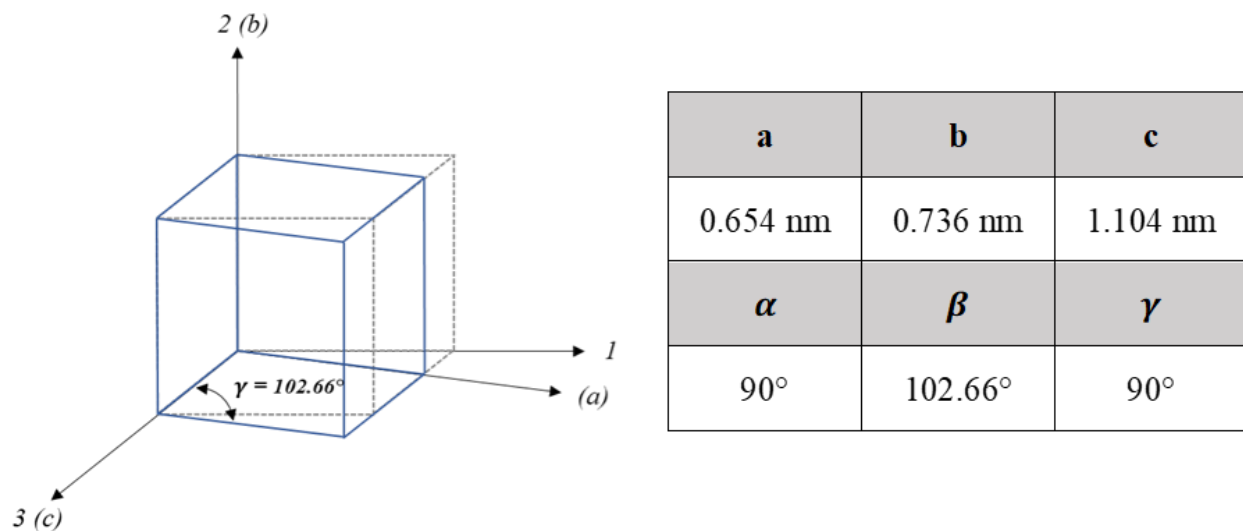


Figure 3.1. Crystallographic axes and unit cell parameters of β -HMX

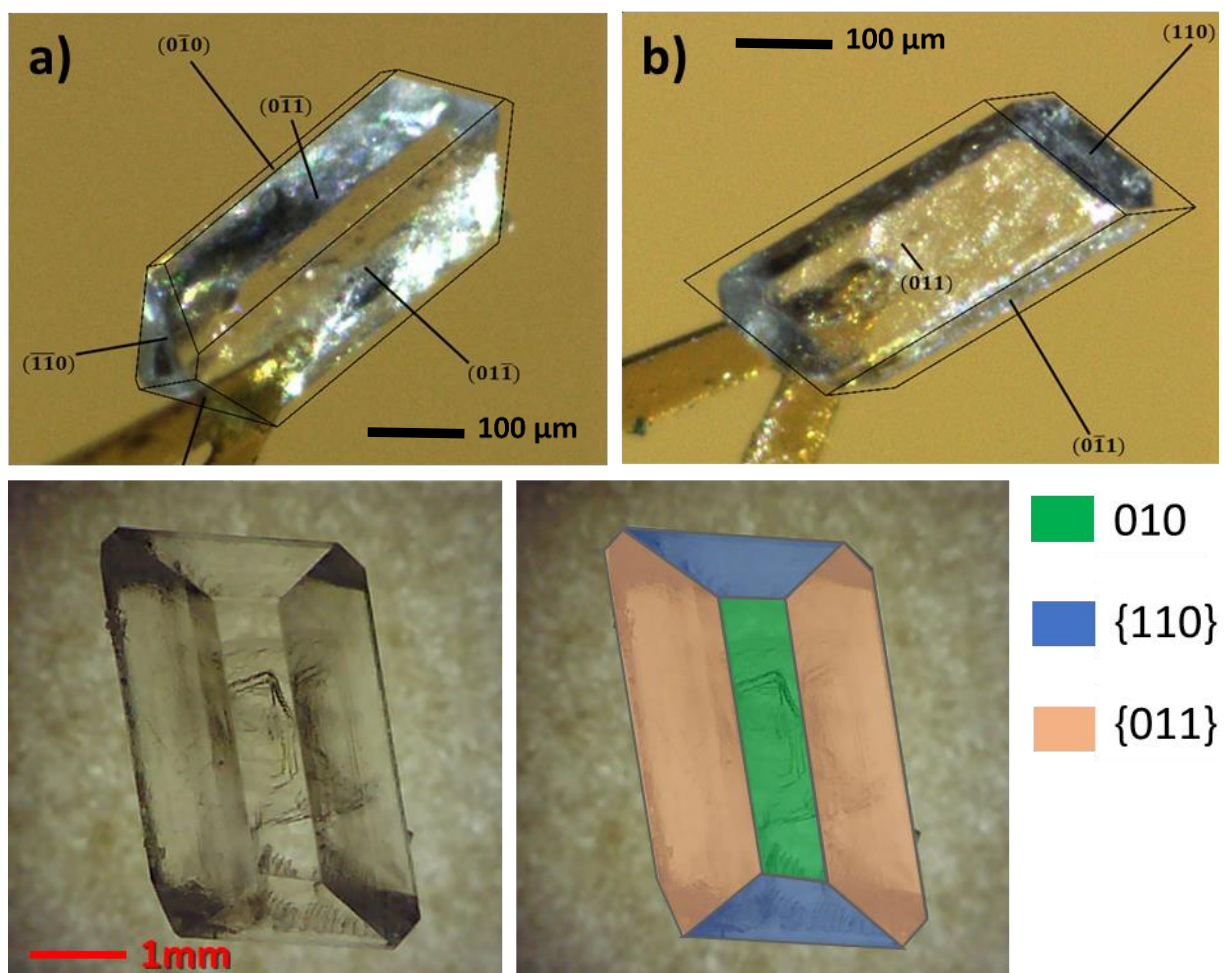


Figure 3.2. Identified orientations of β -HMX crystals: a) morphology 1 b) morphology 2.

For both morphologies, indentations were performed on large areas of the facets corresponding to the $\{011\}$, $\{110\}$ and (010) planes. Typically, crystals chosen for experimentation were on the scale of 1mm or larger in length so as to provide sufficient surface area for multiple indentations.

3.2.2 Nanoindentation

Indentation for this work was performed with a diamond Berkovich tipped conical indenter. Detailed images of the indenter, obtained via SEM, are shown in Figure 3, a NanoTest platform (Micro Materials Ltd., UK), described in previous work (Verma & Tomar, 2014), is used to perform the indentation experiments. The crystals were oriented with the facet of interest perpendicular to the indenter and indentations were separated by a minimum of $100\text{ }\mu\text{m}$ to limit the possibility of coalescence between indents. The orientation of the corners of the indenter relative to the sample orientation was not pre-determined and indentation loads varied from 50 to 200mN.

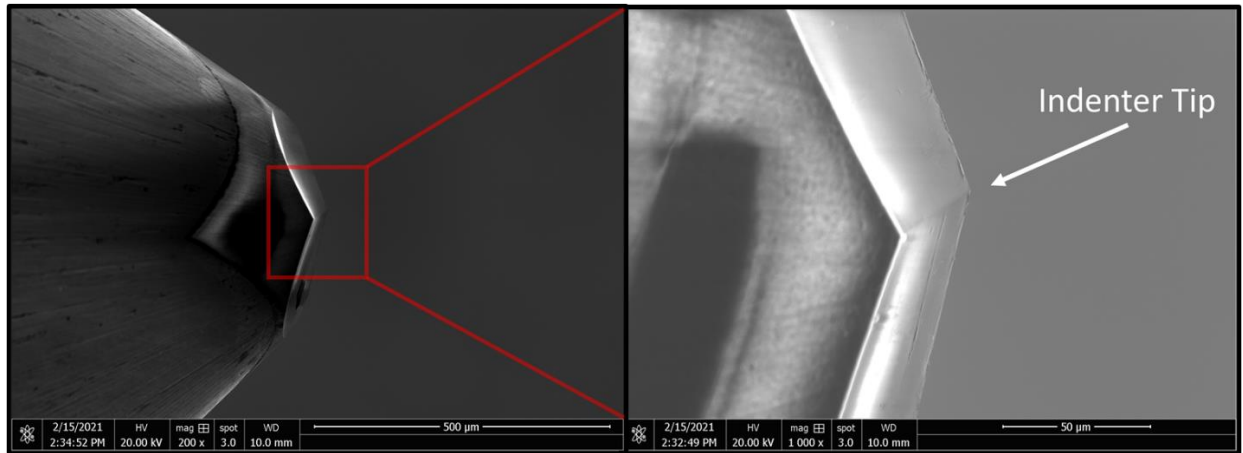


Figure 3.3. Diamond Berkovich tipped conical indenter

3.2.3 Fracture Toughness and Surface Energy

Numerous studies have made employed nanoindentation as an experimental method to evaluate mode I (tensile opening) fracture toughness of materials based on the development and propagation of cracks from corners of the indenters during the loading or unloading stages of indentation. This has proven to be a strong basis for simple and rapid measurement of fracture toughness of materials (Tandon et al., 2015). These previous studies led to the development of models relating fracture toughness to the ratio $(P/c^{3/2})$, where P is indentation load and c is indentation-initiated total crack length as shown in Figure 4. Equation (1) was developed by Lawn et al. (Lawn & Fuller) based on median-radial halfpenny cracking in homogeneous brittle materials:

$$K_{IC} = 0.016 \left(\frac{E}{H} \right)^{\frac{1}{2}} \frac{P}{c^{\frac{3}{2}}} \quad (1)$$

Where E is the Young's modulus, and H is the hardness of the material. However, it has been suggested that this equation is better suited in application to cracks formed by sharp indenters with symmetrical geometry such as Vickers indenters as the indenter is more likely to produce halfpenny cracks (Dukino & Swain, 1992).

Equation (2), developed by Laugier (Laugier, 1987) on the basis of Palmqvist or radial cracking (Figure 4), and modified for Berkovich indenters (Dukino & Swain, 1992), has been proposed as a potentially more appropriate option for Berkovich indenters, which have a nonsymmetric geometry:

$$K_{IC} = (1.073)\chi_v \left(\frac{a}{l} \right)^{\frac{1}{2}} \left(\frac{E}{H} \right)^{\frac{2}{3}} \frac{P}{c^{\frac{3}{2}}} \quad (2)$$

Where a is the length of the indent alone and l is the length of the crack without the indent, therefore c is the addition of l and a as shown in Figure 3.4. Here, chi has been found to be 0.016 for the

Berkovich indenter (Dukino & Swain, 1992). The nonsymmetric geometry of the Berkovich indenter prevents the halfpenny crack from joining two comers of the impression and passing through the center of the indentation and is more likely to develop radial cracks during loading (Dukino & Swain, 1992). Equation (2) is also employed in cases where the value of c/a is greater than 3. In this work, both equations will be used to obtain fracture properties and compared.

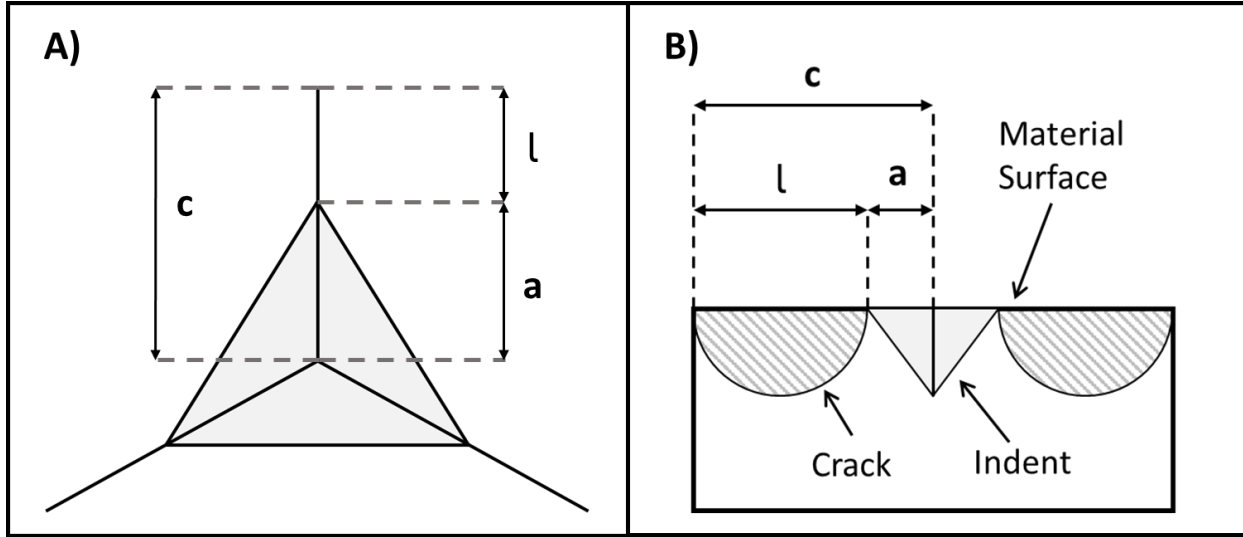


Figure 3.4. (A) Top view of indenter with radial cracks (B) Side view of indents with radial cracks

Fracture surface energy is obtained through Griffith's criterion relating surface energy to fracture toughness for brittle materials:

$$\gamma_s = \frac{K_{IC}^2(1 - \nu^2)}{2E}$$

Using the methods detailed above, we aim to study the orientation dependence of fracture toughness and surface energy in β -HMX crystals. The cleavage plane for β -HMX crystals has been primarily found to be the $\{011\}$ family of planes (Dick et al.; Palmer & Field), and this is also observed in this study. Therefore, the fracture properties obtained from this work are primarily for the mode I fracture behavior of the $\{011\}$ family of planes when loaded from different orientations.

3.3 Results and Discussion

Indentation experiments were carried out on the (010), {011}, and {011} planes of selected crystal samples, and the cracks were measured visually via optical microscope. Images of residual indentations on the (010) plane at increasing load, and the resultant cracking, is displayed in Figure 3.5 below.

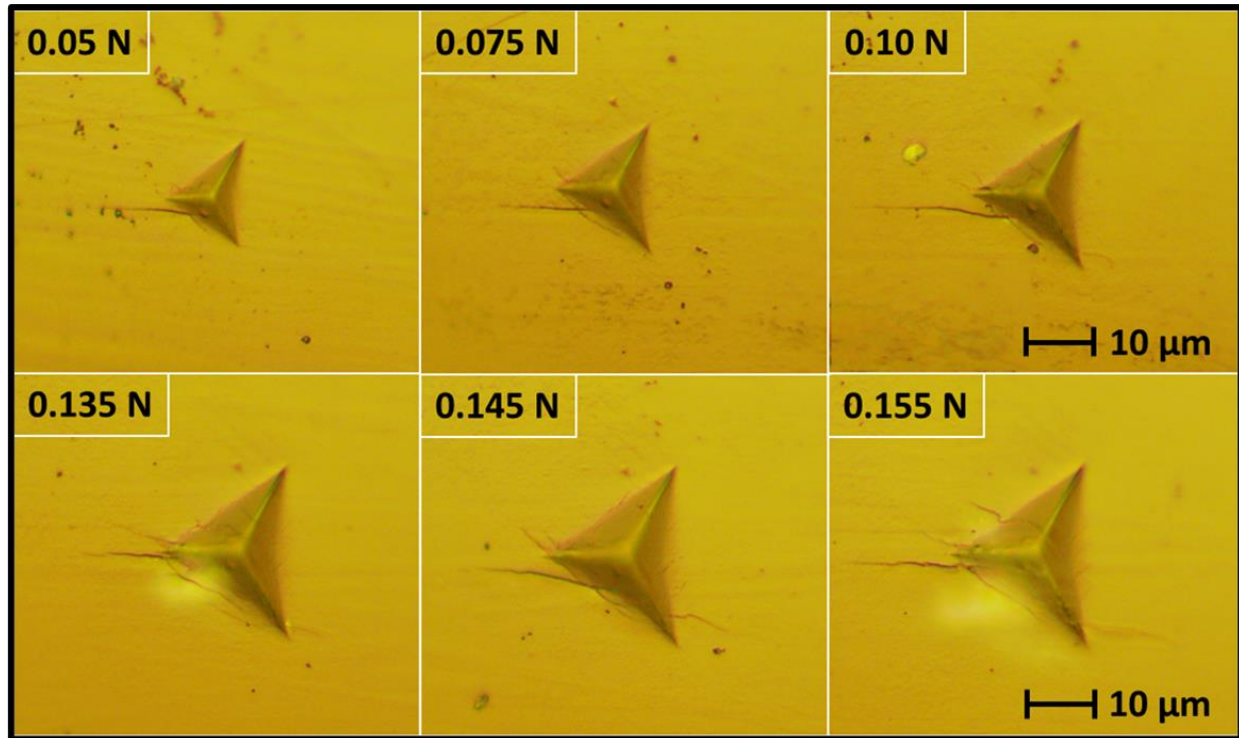


Figure 3.5. Imaged indentations performed on the (010) facet of a β -HMX crystal

A notable observation is that the radial cracks on the (010) and the {110} facets did not originate at the corners of the indents, this has also been indicated in other studies (Burch et al., 2017). The load to crack length relationships for indentations on the different facets is presented in Figure 3.6. Overall, the indentations on the facet aligned with the {110} plane presented longer crack lengths at lower loads and was the only orientation to have average c/a values larger than 2.5.

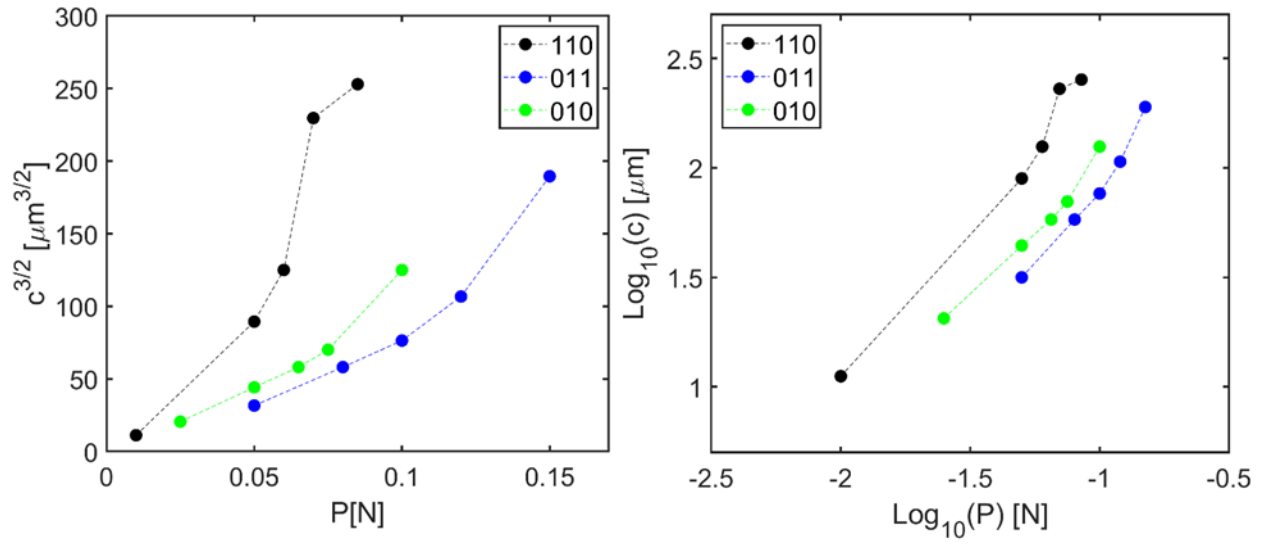


Figure 3.6. Load vs crack length comparison for 3 facets

The log-scale plots of crack length versus load yielded mostly linear behavior with a slope of approximately 0.95, a value which is higher than the value of 0.66 projected for more brittle ceramics. The cracks formed on the facets corresponding to the (010) and {110} planes predominantly grew along the {011} cleavage, this was also an expected outcome (Dick et al., 2004). Slip presented on the surface of the crystal at indentation loads above 50mN, this is clearly shown for indentations on the (010) facet in Figure 3.7. Due to the approximate angle of the slip planes, it is speculated that these are the (101) slip planes as identified by Dick et al. (Dick et al., 2004)

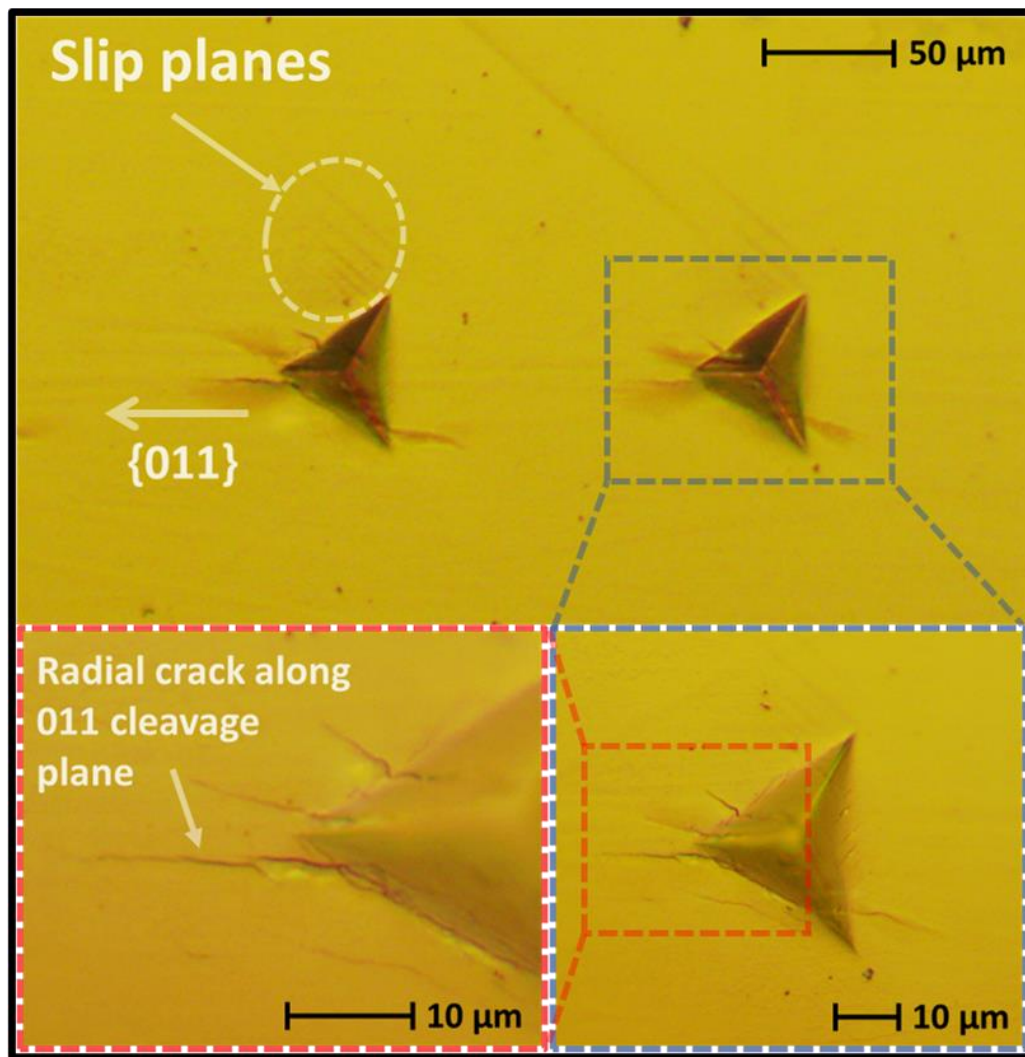


Figure 3.7. Slip planes and cracking along cleavage planes for indentation on (010) facet

Fracture toughness and fracture surface energy for all planes were calculated based on using both Equation (1), Lawn's model, and Equation (2), Laugier's model. The results for both models are shown in below plotted against indentation load.

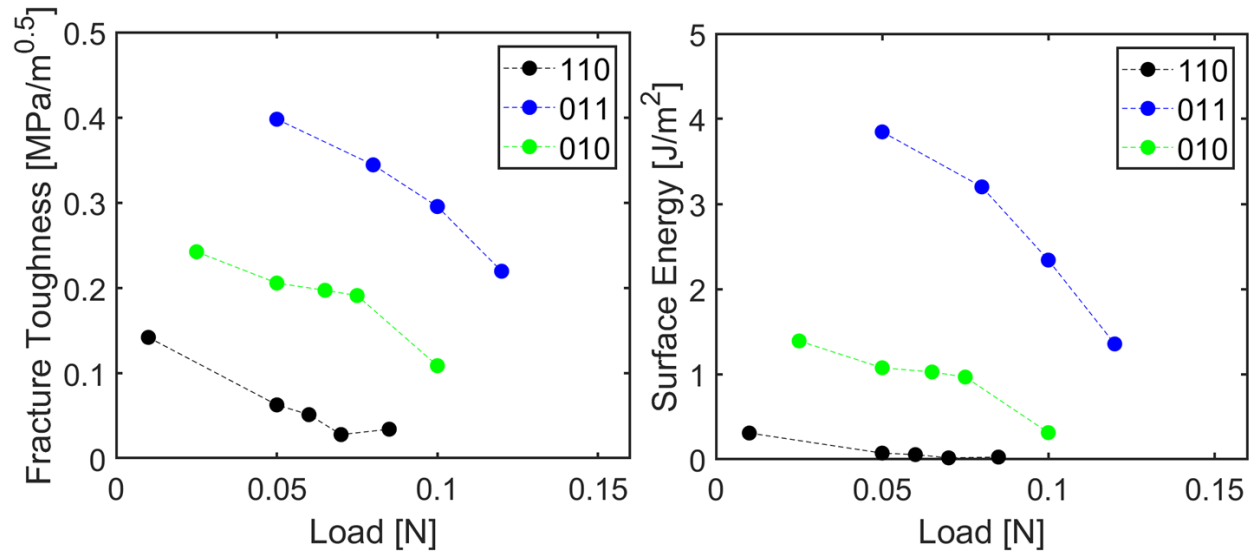


Figure 3.8. Comparison of anisotropic fracture toughness and surface energy vs load using Laugier's model

For the results obtained by Laugier's model, presented in Figure 3.8 above, a decrease can be observed in both fracture toughness and surface energy with an increase in load. The {011} facet presented the heaviest dependency on loading and deformation as the variation in measured values was quite high. Other facets showed variance in values, but their slopes were comparatively flatter. A possible explanation for the large variation observed could be the presence of significant sub-surface cracking upon indentation loading of the {011} facet. This can be observed in Figure 3.9, in the (a) portion of the figure, it is observed that the surface cracking extends radially out from the indentation corners as expected however, at first it seems the extent of cracking is not significant. The image in the (b) portion of the figure is of the same indentation imaged with a different optical microscope. This image clearly shows the presence of extensive subsurface cracking. This can be observed as a darkened area on the (a) portion of the figure.

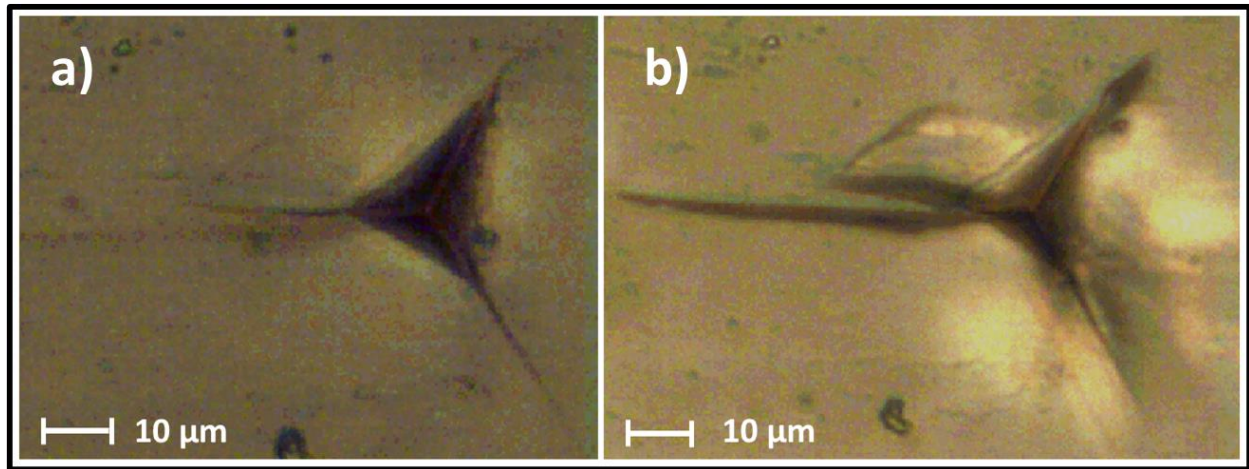


Figure 3.9. Sub-surface cracks developed upon indentation loading on $\{011\}$ facet

The potential causes of these crack behaviors were not fully understood as such indentations with extensive sub-surface cracks, usually at higher loads, were omitted from analysis. The values obtained for fracture toughness, particularly for the 010 plane, appear to be close to results presented by Burch et al. (Burch et al., 2017), in which Laugier's model was also used. The values for the other planes are either higher or lower however, due to the variance in values, an averaged value for the 011 plane was not obtained. Overall, the results from Laugier's model gave higher results for both fracture toughness and fracture surface energy.

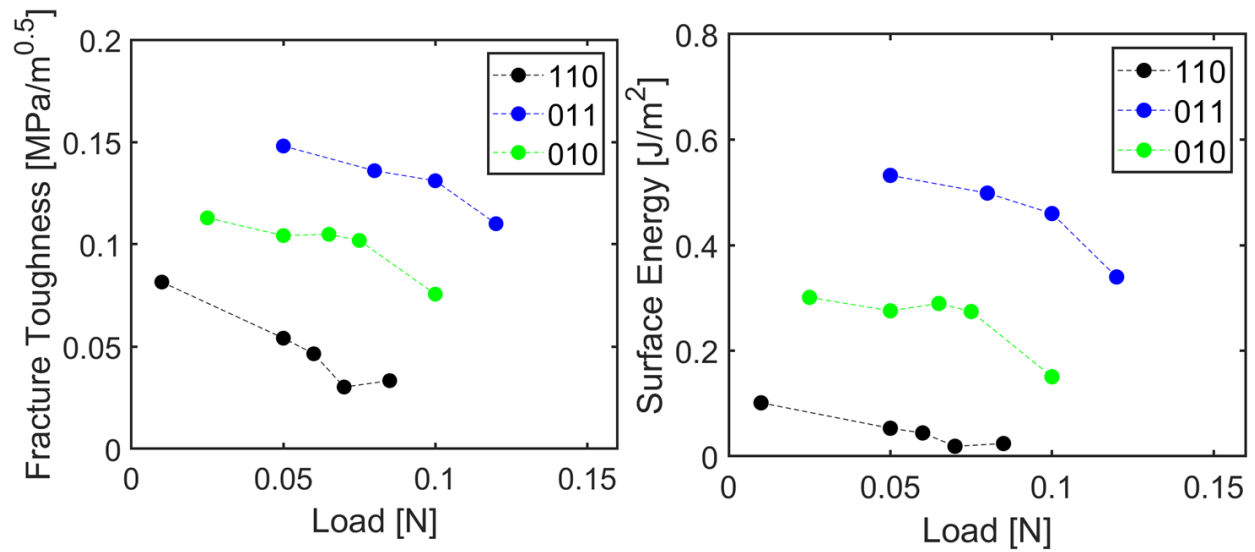


Figure 3.10. Comparison of anisotropic fracture toughness and surface energy vs load using Lawn's model

Results obtained by Lawn's model are presented in Figure 3.10 above. Lawn's model produced significantly lower values and less variation than Laugier's, especially for the 011 plane. Due to this, we will be presenting the results using Lawn's equation as the final results. Both the distribution for fracture surface energy and fracture toughness were similar to value obtained for specific planes by Palmer and Field and Wang et al. The finalized values were tabulated and presented in Table 1 below. The tabulated values include the smallest angle between the listed plane and the cleavage plane, as well as the hardness values obtained in a previous work for each plane. Hardness is listed as it has been found to also be correlated to EM sensitivity (Harris et al., 1982).

Table 3.1. Anisotropic fracture toughness and surface energy values (Lawn's model)

Plane	Angle*	K_{IC} [MPa/m ^{0.5}]	γ [J/m ²]	H [GPa]
010	34°	0.1 ± 0.01	0.26 ± 0.04	0.48
110	51°	0.049 ± 0.02	0.048 ± 0.03	0.56
011	69°	0.12 ± 0.03	0.4 ± 0.13	0.26

*Smallest angle between plane and {011} cleavage planes

The results presented for the fracture properties present clear anisotropy in the fracture behavior of β -HMX crystals. In terms of specific orientation behavior, the values agree with previous values of hardness obtained. The {110} plane which had the highest value of hardness also had the smallest values of fracture toughness and surface energy, which is as expected. Conversely the {011} plane had the lowest value of hardness and the highest values of fracture toughness and surface energy. These findings give some insight into the anisotropic response of the crystal to loading such as impact as a range of expected behavior can be established.

As a final comparison of both models, we graphically compared the fracture toughness to $P/c^{3/2}$ to obtain the constant value of (E/H) for the material. This plot is presented in Figure 3.11 below. From the slope of the plot, we calculated (E/H) for the fitting Lawn's model to be 35.6.

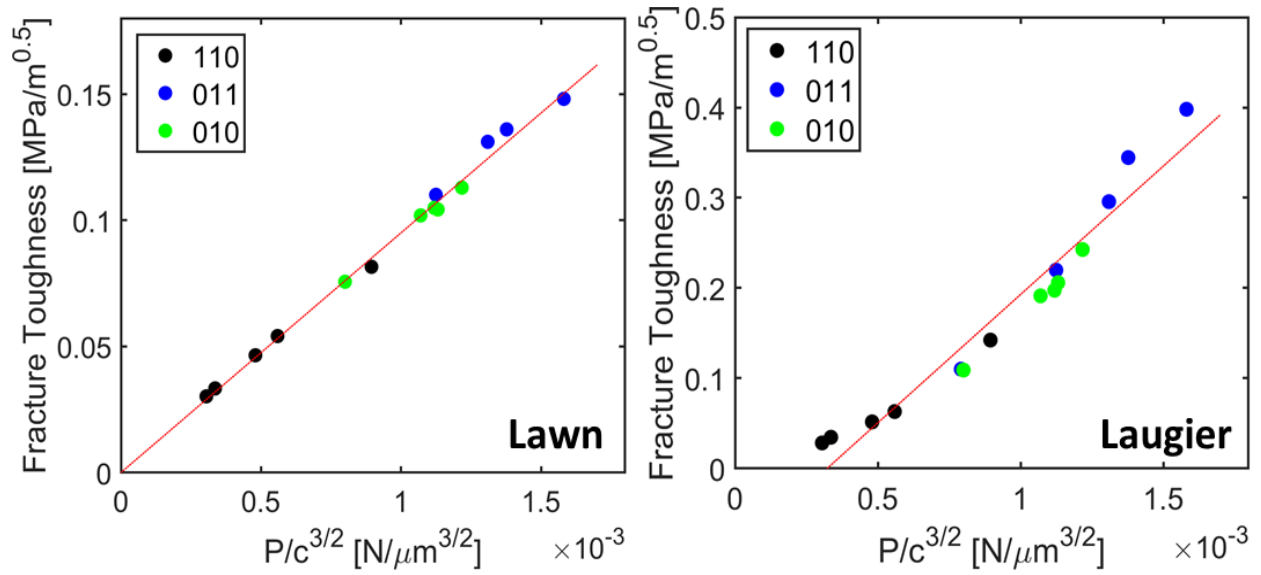


Figure 3.11. Comparison of Fracture toughness vs $P/c^{3/2}$ for both models

Our results using Laugier's model did not fit as well into a linear model, presenting more of a power fit. This is due to the nonlinearity of the $(a/l)^{1/2}$ term with increasing load. This would appear to be confirmed by Dukino and Swain as in their work. They found fracture toughness was not proportional to $P/c^{3/2}$ for cracks which had c/a values less than 2.5. This was attributed to Vickers indenters as they generally create smaller cracks than Berkovich indenters, however it appears the lack of proportionality is applicable to this work with a Berkovich indenter as well.

3.4 Conclusions

In this work, anisotropic values of fracture toughness and surface energy were experimentally obtained to describe the anisotropic fracture behavior of β -HMX. They were calculated by fitting two different models, Lawn and Laugier, and compared. The fitted values were obtained for each plane through nanoindentation experiments at varying loads. We found the Lawn model to produce more satisfactory results as the variance in values was lower and results obtained closely matched those presented in literature. It was found that the $\{011\}$ and $\{110\}$

planes had the highest and lowest fracture toughness respectively and the same is found for surface energy. These values may create a basis for ranges of expected behavior of HMX material for which the orientation may not be readily gaged. The value (E/H) regardless of orientation of β -HMX was found, by Lawn's model, to be 35.6.

4. EXAMINATION OF LOCAL MICROSCALE-MICROSECOND TEMPERATURE RISE IN HMX-HTPB ENERGETIC MATERIAL UNDER IMPACT LOADING

Ayotomi Olokun¹, Bing Li¹, Chandra Prakash², Zhiwei Men³, Dana D. Dlott³, and Vikas
Tomar^{1*}

¹School of Aeronautics and Astronautics, Purdue University, West Lafayette, IN 47907,
USA

²Department of Civil Engineering, Johns Hopkins University, MD 21218, USA

³Department of Chemistry, University of Illinois at Urbana-Champaign, IL 61820, USA

*Corresponding Author, **Email:** tomar@purdue.edu, Tel: 765-494-3423

Abstract

This work presents direct measurements of temperature distribution during impact loading of Cyclo-tetra-methylene-tetra-nitramine (HMX) - Hydroxyl terminated polybutadiene (HTPB) material at mesoscale with sub-microsecond/micrometer resolution. The focus is on analyzing the effect of impact loading influence on microstructure dependent material behavior. The temperature distribution is shown to be strongly correlated to local material microstructure with interface and particle shape playing a key role.

Keywords: Drop Hammer, Microsecond and micrometer scale temperature measurement, Energetic Materials

4.1 Introduction

A typical energetic material (EM) mixture with approximately 60% to 95% solid oxidizer material (e.g. Cyclo-tetra-methylene-tetra-nitramine (HMX)), and a polymeric binder (e.g. Hydroxyl terminated polybutadiene (HTPB)), is normally designated as polymer bonded explosive (PBXs) (David J. Benson & Paul Conley, 1999). Due to complex microstructure, such materials can have abrupt temperature rise at any location within the EM microstructure under external impact that may lead to unintended detonation. Such regions within the EM microstructure are known as ‘hot-spots’. The hot-spots are known to be responsible to start chemical reaction within the microstructure leading to detonation (David J. Benson & Paul Conley, 1999). It is important to investigate the effect of oxidizer particle size, volume fraction, hot-spot threshold temperature, and time span necessary to cause initiation of detonation (Field, 1992). Rae et al. (Rae, Palmer, Goldrein, Field, & Lewis, 2002) have observed that the debonding of interfaces in PBXs contributes significantly to temperature rise. Prakash et al. (Prakash, Olokun, Emre Gunduz, et al., 2019) have shown that the interface chemical composition of EM determines the impact induced fracture resistance and strength. Drodge et al. (Drodge & Proud, 2009) have shown that an increase in particle size of EM microstructure decreases the yield strain of overall material. The effect of particle size on the overall behavior of energetic materials has also been studied by Tan and coauthors (Tan, Huang, Liu, & Geubelle, 2005). It was observed that the oxidizer particle size affects the hardening behavior as well as the particle-matrix debonding. Prakash et al. (Prakash, Gunduz, et al., 2018) and Zhou and Co-workers (A. Barua, Horie, & Zhou, 2012; Ananda Barua, Kim, Horie, & Zhou, 2014) have studied impact induced behavior of various idealized microstructure of PBXs using cohesive finite element method (CFEM). However the numerical and experimental techniques used to study the deformation behavior of energetic materials under

different loading conditions employ techniques that cannot measure local temperature under impact at microstructural length scales. This work presents one such experimental technique and relates the measurements with a set of simulations performed earlier.

4.2 Method

The fundamental imaging is performed during a drop hammer test. The drop hammer test is one of the easiest ways of assessing the mechanical response and sensitivity of particle-sized explosives to impact. It involves impacting a material sample with a hammer and striker to subject it to a high-speed compressive load and in the case of energetic materials, this load is sufficient to cause impact induced ignition. In this work, we aim to observe and characterize the properties, particularly temperature, of energetic materials before, during, and after ignition. One challenge in analyzing the temperature evolution of EM during impact is to obtain measurement with high spatial and temporal resolution. At this time, no single thermal imaging detector can provide both (Men, Bassett, Suslick, & Dlott, 2018). Here, this obstacle was overcome by using two different kinds of thermal imaging cameras: a mid-wavelength infrared (MWIR) camera (mid-range infrared 3.7- 4.8 μm) and a thermal imaging camera with a linear array of 32 HgCdTe (MCT) detectors developed by Men et al (Men et al., 2018). The MWIR camera is located beneath the sample, and it has a 640*512-pixel detector array, which can provide a near-diffraction limited spatial resolution of 15 μm . The MWIR camera is triggered at the frequency of 100 Hz, after receiving each trigger signal the MWIR camera obtains one visual representation of the energetic material temperature change, and the imaging process continues until the maximum frame of 50 is reached. The limit of the MWIR camera is that it has an inter-frame interval limit of 8.3 ms, which would compromise information on temperature changing during the transient explosion of

EM, and this can be solved by using another camera with linear array infrared detector working with the MWIR camera. Compared with the MWIR camera, the linear array camera has higher time resolution due to simplicity in temperature acquisition with 1-D detector array. With an array of 4 MHz analog to digital converters, the camera can acquire the temperature of 32 data points every 250 ns on the sample spanning a length of about 3 mm. In terms of the frame rate, the linear array camera is about 40000 times faster than the MWIR video camera, which can provide detailed analysis on initiation, development and attenuation of heat generation in EM explosion with nanosecond resolution. The data acquired is then presented as a 3-dimensional waterfall plot (shown in results).

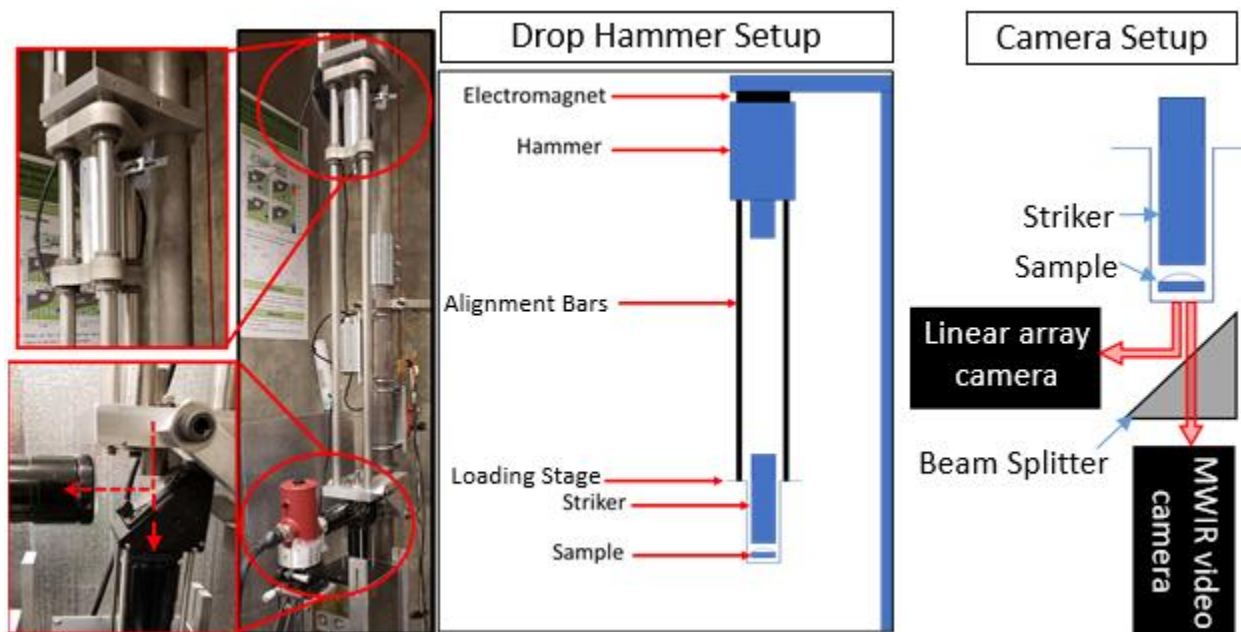


Figure 4.1. Experimental Setup. Left: drop hammer impact setup, right: infrared camera setup for temperature acquisition

The setup used in this work can be seen in Figure 1. The setup employs a simple mechanism involving a 4 kg hammer suspended by electromagnet at a height of approximately 1m above a sample, secured in a loading stage, beneath a cylindrical striker. The hammer is dropped vertically,

with the aid of frictionless alignment bars, onto a striker, roughly the same diameter as the sample holder, which impacts the material sample in the loading stage. As the hammer drops, it passes a photo sensor which, coupled with a delay generator, generates a signal which triggers the cameras to continuously capture images at a set frequency for a set amount of time.

4.3 Results

In many cases, the energetic material will ignite due to localization and concentration of the impact energy at ‘hot spots’, which are regions in the microstructure of energetic materials which have a sufficient size and temperature to start the chemical reactions that cause initiation or detonation. Void collapse, frictional heating, crack tip heating, are some of the energy localization mechanisms responsible for ‘hot-spots’ creation, that have been suggested in literature (Field, 1992). A recent study (Men et al., 2018) on the impact induced temperature behavior of a polymer-encased single crystal HMX showed that the initiation occurs due the plastic deformation and crack formation as well as frictional dissipation. One of the main concerns in these materials is the frictional heating that occurs among the crystals due to their proximity to each other. Such phenomenon can get more pronounced depending on the density of crystals because of the increase in the frictional effect between crystals during impact induced deformation. Impact induced failure and temperature rise behavior of an HMX based polymer bonded explosive has been studied using a cohesive finite element method (A. M. Olokun et al., 2020). It has been observed that the concentration of crystals plays an important role in determining the energy localization within the microstructure. The shear forces between crystals as well as that between crystal and binder was shown to increase the localization of energy dissipation in these regions. Such energy localizations were found to be of significant intensity at the polymer-crystal interface, especially in the regions

where crystal density was high. It was also found that the crystal fracture was the primary failure under high velocity impact which significantly increased the temperature in failed crystals. In this work, our goal is to investigate the effect of crystal proximity and crystal failure on the temperature rise and initiation in polymer encased HMX crystals.

The sample used in this work is shown in Figure 2. Four crystals with varying distance between them were placed along a line. The first two crystals are closer to each other than the other two. The results of a drop hammer impact test on HMX particles in a polymeric binder are shown in the images below.

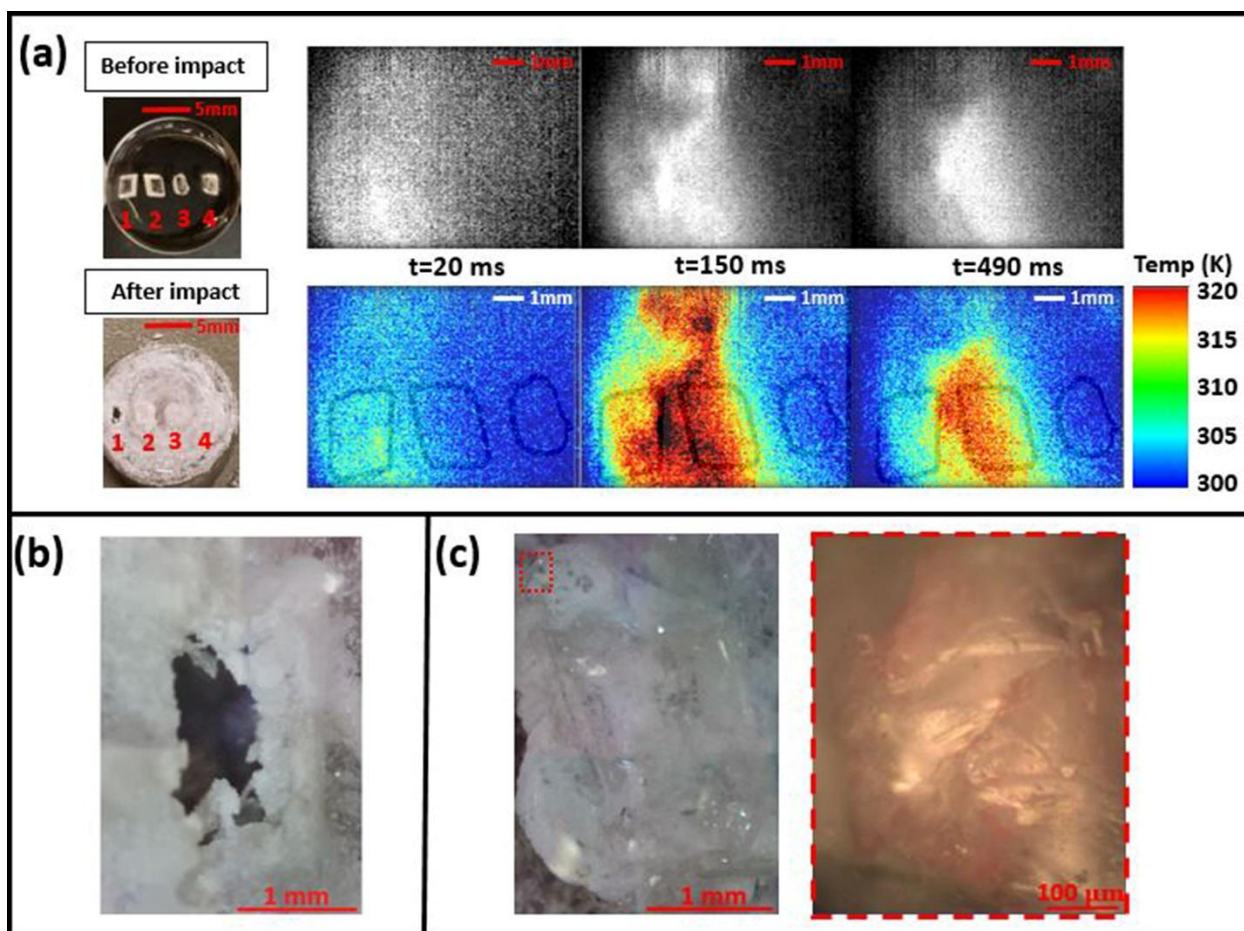


Figure 4.2. (a): Temperature map of HMX particle ignition under impact with HMX particle profile: ignition initiation ($t=0.02$ s, $t=0$ s for hammer impact), ignition ($t=0.15$ s) and post ignition ($t=0.49$ s); (b): Post impact interface debonding of crystal 1; (c): Post impact fracture of crystal 2.

Table 4.1. Microstructure Character of Energetic Material Crystals

Particle No.	Inertia angle				Distance to adjacent partials		
	Top, left	Bottom, left	Top, right	Bottom, right	Minimum distance	Left side center spacing	Right side center spacing
1	102°	79°	80°	112°	0.6 mm	-	2.9 mm
2	78°	100°	102°	80°	0.6 mm	2.9 mm	2.8 mm
3	80°	Blunt corners			0.9 mm	2.8 mm	3.0 mm
4	85°	102°	90°	78°	1.5 mm	3.0 mm	-

The microstructure characters of the EM crystals including crystal shape and distance between the crystals are summarized in Table I. Based on the work of Tan et al., during high strain rate loading of polymer based composite with EM particles, coarse particles were more prone to interface debonding and catastrophic explosion (Tan et al., 2005). In the work of Olokun et al., finite element analysis with cohesive zone model showed that for EM mixture under impact, local energy dissipation was more severe for samples with higher content of EM crystals due to the high interaction level between particles (A. M. Olokun et al., 2020). Besides, HTPB- HMX interface was also observed to be prone to debonding in the numerical simulation due to the high-level stress gradient and stress concentration at the interface (A. M. Olokun et al., 2020). As the result, the interface of coarse crystals in the region with high EM concentration was most critical during the impact test. Among the four EM crystals in the sample, particle 1, 2 and 4 had sharp corners; and particle 1 and 2 had the lowest distance to the adjacent particle, exposing them to high level impact energy concentration and interaction between particles (A. M. Olokun et al., 2020). Thus the sharp corners of particle 1 and 2 were expected to be the hot- spot of detonation during the impact, and this was verified by the temperature history observed from the MWIR camera shown in Figure 2

(a). After 20 ms of impact, crystal 1 and 2 started to show a temperature rise. Although the hammer impact was centered at the middle of the encasing, the temperature increased at a single crystal near the periphery. The detonation initiated at the polymer- EM crystal interface of particle 1, propagated along the interface and then propagated to crystal 2. This can be attributed to two main reasons. One, due to the variation in the roughness of the crystal surfaces, the frictional effect between the crystal and the polymer was more concentrated at this crystal. As crystal 1 and 2 had sharp corners and low mutual distance, high level frictional heat was generated at the shear banding near the crystal- polymer interface (Field, 1992). A stripe with high temperature along the crystal- polymer interface of crystal 1 and 2 was presented in the infrared images captured by MWIR camera in Figure 2 (a). And two, the energy localization was promoted by the crystal fracture and interface debonding occurred at this position, which is shown in Figure 2 (b, c). The initiation of crystal fracture at this position can be explained based on the work of Olokun et al. (A. M. Olokun et al., 2020), where the numerical impact simulation of HMX based EM showed that the higher proximity of crystals increases the stress localization which may result in crystal fracture. Next the energy localization due to the crystal fracture initiates the detonation, Figure 2, around 150 ms. It can be seen from Figure 2 that at the time of fracture, the temperature rises throughout the crystal and spreads outwards towards the second crystal. However, the low thermal conductivity of the polymer prevents the temperature in the second crystal to rise significantly. The sample, after impact, shows that the explosion completely consumed the crystal and the temperature drops afterwards. Although the MWIR camera images provide the location of high temperature region, it cannot resolve the short time duration of the detonation period. A more detailed temperature rise history along the sample can be studied using the linear array camera shown in Figure 3.

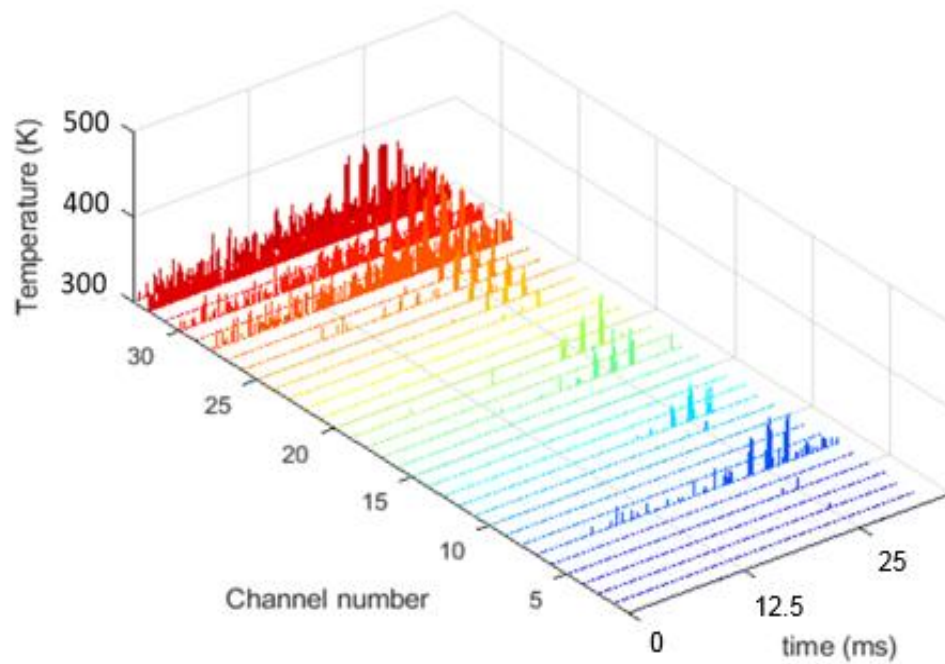


Figure 4.3. Temperature-time profile of impact showing different channels in different colors

The temperature history in Figure 3 shows that the actual temperature was high (around 380 K) during the detonation. It also shows that the temperature rise was confined in the single crystal and the farther away from the first crystal, the temperature did not rise significantly to start the initiation. The comparison of the temperature maps with the temperature history in Figure 4 shows the location and time of the detonation. The detonation initiation starts around 22 ms and the temperature rises to the highest value in 2-3 ms and reaches a maximum at around 25 ms. It again starts to decrease and drops to a lower value in around 5 ms.

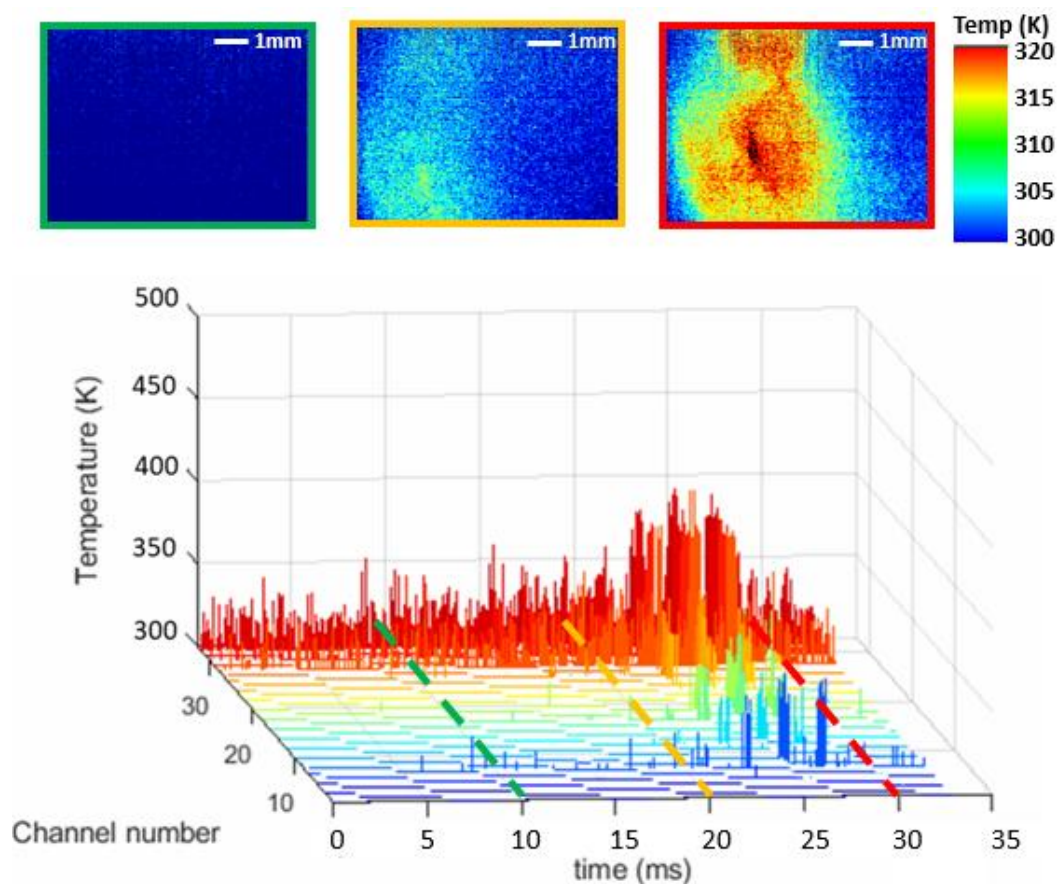


Figure 4.4. Location of the temperature maps on the time profile

The temperature rise time from the start of impact and the maximum temperature is lower than that of the decrease of temperature after the explosion. Also the temperature during the explosion near the second crystal increases but again decreases very fast which prevents any initiation.

4.4 Conclusion

In this work the effect of HMX crystal failure and crystal proximity on the impact induced local temperature rise was studied. A drop hammer impact setup was used to impact the sample. Four HMX crystal encased in a polymer was impacted and the temperature change was recorded using two cameras. One MWIR imaging camera showed the local position of the temperature rise

and the failure behavior of crystals. It was observed from the infrared imaging that the crystal failure occurs where the crystal proximity is higher, and this matched the prediction of previous experimental and numerical analysis [(Field, 1992), (Tan et al., 2005), (A. M. Olokun et al., 2020)]. In order to quantify the effect of crystal proximity, large number of tests with varying crystal distance and sizes have to be performed which will be done in a later article. Second linear array camera showed a nano-second resolution time dependent temperature profile along the sample. The results showed a higher temperature rise time to the initiation and detonation than the temperature decrease after the detonation. The after-impact picture of the sample shows that the detonation completely consumed the crystal where the detonation occurred whereas other crystals remain unaffected. Stripe region with high temperature along the crystal-polymer interface was observed, which was contributed to the shear banding and interface debonding at this location.

5. COHESIVE FINITE ELEMENT MODELING OF THE EFFECT OF PARTICLE ANISOTROPY ON THE MECHANICAL RESPONSE OF IMPACT LOADED HMX-BASED PBX MICROSTRUCTURE

Ayotomi M. Olokun¹, Meghana Sudarshan¹, Tyler Dillard¹, Vikas Tomar^{1*}

¹ School of Aeronautics and Astronautics, Purdue University-IN, 47907, USA

*Corresponding author, **Phone:** (765)-494-3423 **Email:** tomar@purdue.edu

Manuscript under preparation.

5.1 Introduction

Polymer-bonded explosives (PBXs) are a class of energetic material (EM) which consist of a relatively high percentage of solid oxidizer material particles embedded in a polymeric binder. Cyclo-tetra-methylene-tetra-nitramine (HMX), a relatively insensitive nitroamine explosive, is used in a large class of PBXs as solid propellant and explosives. The microstructure of HMX-based PBX is known to be complex in terms of behavior and response to stimuli. Inhomogeneities in the microstructure of PBXs such as material boundaries, varying particle density, voids, etc., can create localized areas of high temperature known as “hot spots”, as a response to external environmental stimuli such as impact (David J. Benson & Paul Conley). Some mechanisms that have been shown to initiate hot spots include the adiabatic compression of trapped gas in the microstructure, particle fracture, viscous heating of surrounding material, etc. These hotspots are the main phenomena that lead to detonation of EMs and as such, their initiation conditions and parameters need to be studied in order to accurately predict the behavior of EMs when exposed to different stimuli.

For various forms of deformation, the material properties and response of HMX, particularly β -HMX (Gallagher et al., 2014), has been shown to be dependent on orientation (Baer, 2002). Fracture behavior is one of the responses of HMX crystals known to be orientation dependent due to the anisotropic nature of the crystal. Deformation, such as slip and fracture, have been found to occur on specific planes of the crystal depending on which orientation the crystal is loaded (Dick et al., 2004; Palmer & Field, 1982). As such, it follows that; as EMs are made up of anywhere from 60% to 90% of oxidizer particles, the orientation dependence of HMX crystals could potentially play a crucial role in accurately predicting the behavior of the overall PBX material.

Impacts on energetic materials, even at lower velocities, can lead to weak shocks in the material which build up as stress concentrations and local temperature rises in the microstructure. Prediction of the impact induced temperature rise in a HMX based energetic material requires the knowledge of material models to simulate the deformation behavior, such as the relevant constitutive model, fracture failure model, and various thermal properties (Prakash, Emre Gunduz, et al., 2018).

Currently, with few exceptions, simulation of the mechanical behavior of HMX-based energetic materials in the mesoscale generally overlooks the anisotropic properties of the material, however the argument can be made that incorporation of anisotropic properties of HMX crystals may improve the current ability to predict the behavior of these materials. In one example, Conroy et al. (Conroy et al., 2008) modeled the behavior of β -HMX crystals by measuring the anisotropic principal stresses via first principles density functional theory. Their results were reported to adequately match existing experimental data. Wang et al. (X. Wang et al., 2017) made use of a full field method with a combination of viscoelastic and elasto-viscoplastic models to simulate the

local damage behavior of HMX-based energetic materials. Work by Zamiri et al. (Zamiri & De, 2011) used experimental data to model the plastic response of anisotropic HMX crystals. Along similar lines, this work aims to use previously measured anisotropic material properties to model the response of HMX-based PBX microstructure to mechanical stimuli. The isotropic and anisotropic models are also compared to study the extent of the effect of anisotropy in the model.

5.2 Method

5.2.1 Cohesive Finite Element Model

The cohesive zone model-based finite element method (CFEM) is a technique used to quantitatively analyze the fracture behavior of a material through explicit simulation of fracture processes (Prakash, Olokun, Emre Gunduz, et al., 2019). In this work, a 2-D model of a digitized PBX microstructure is generated, which is a modified version of the microstructure used in work by Dai et al (Dai, Lu, Chen, & Chen, 2019), generated by the application of Voronoi tessellation. The microstructure is assumed to be a relatively small section of a larger whole microstructure, and as such, the CFEM framework assumes plane strain. Cross-triangle shaped elements, shown in Figure 5.1, are used to define the mesh of the model, each element with cohesive surfaces specified along all element boundaries. The simulated sample is $100\text{ }\mu\text{m}^2$ with an average element size of $5\text{ }\mu\text{m}$, and the sample mesh contains a total of 160,000 triangular elements. Here we make use of a Newmark β method-based time integration scheme and the average time step is chosen based on Courant-Freidrichs-Lewy criterion (Zhai & Zhou, 2000). This cohesive finite element framework has been incorporated in previous works to successfully model behavioral responses of EM microstructures (A. M. Olokun et al., 2020; Prakash, Gunduz, & Tomar, 2019b).

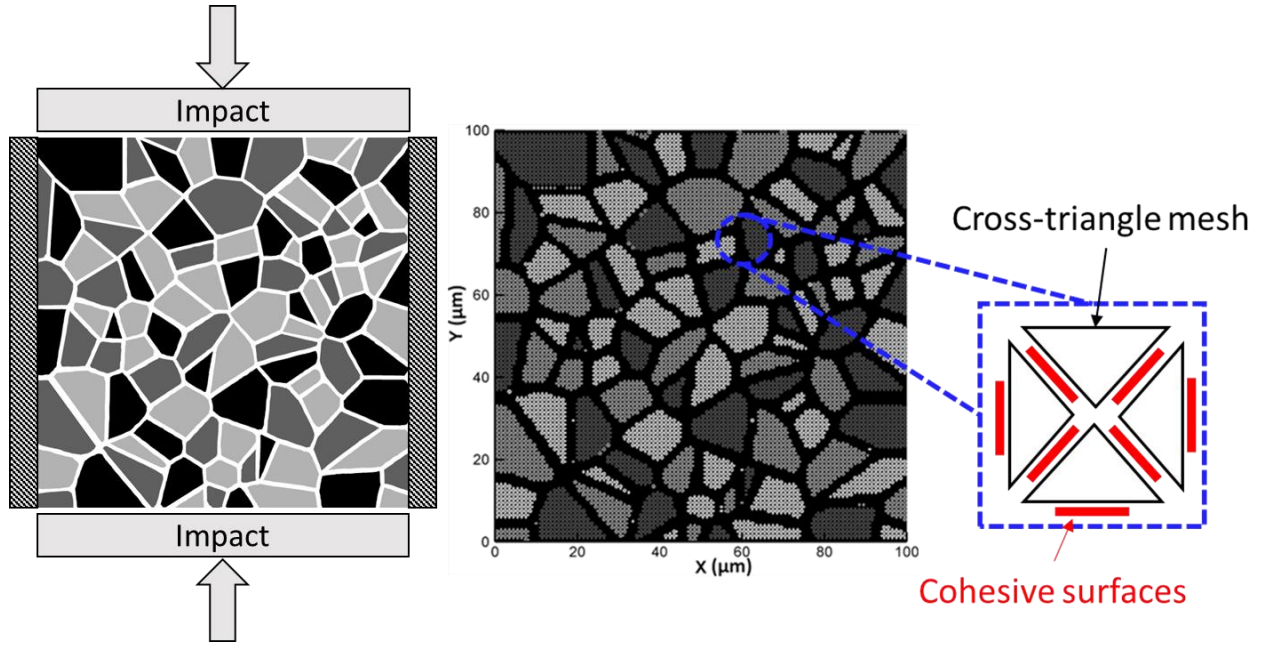


Figure 5.1. Finite element model showing boundary condition, loading configuration, and cross triangle mesh.

For the continuum elements, elastic and viscoplastic constitutive models are used to govern the stress-strain relations (Prakash, Gunduz, & Tomar, 2019a), and comparison of the value of equivalent stress to yield stress determines the non-elastic behavior threshold.

$$\sigma_{eq} = \sqrt{\frac{3}{2} \tau'_{ij} \tau'_{ij}}, \text{ where } \tau' = \tau + p$$

The Mie-Gruneisen equation of state is used to calculate pressure:

$$p = K\phi + A\phi^2 + B\phi^3 + \gamma(1 + \phi)e \quad (1)$$

where,

$$\phi = \frac{\rho}{\rho_0} - 1.$$

where, K is the bulk modulus, A and B are Hugoniot curve parameters (David J. Benson & Paul Conley), γ is the Gruneisen parameter, ρ_0 is the initial density, and e is the internal energy per unit volume. These parameters are obtained from literature and presented in Table 5.1 below.

Table 5.1. Mie-Gruneisen parameters for HTPB and HMX

	K (10 ⁵ MPa)	A (10 ⁵ MPa)	B (10 ⁵ MPa)	γ	ρ_0 g/cm ³
HTPB (Lee et al, 1997)	0.02	0.294	0.0196	0.7	0.9
HMX (Hwang et al, 2014)	0.125	0.22	0.15	1.03	1.9

As the loading is compressive in nature, in order to prevent interpenetration between elements, a penalty-based exponential relation between traction and separation is used (Prakash, Gunduz, et al., 2018).

Table 5.2. Cohesive parameters for HTPB and HMX

	Cohesive Strength (MPa)	Critical Displacement (mm)	Cohesive Energy (N/mm)
HTPB (Prakash, Olokun, Emre Gunduz, et al., 2019)	0.8	0.5	0.2
HMX (Prakash, Olokun, Emre Gunduz, et al., 2019)	100	5x10 ⁻³	0.25

The underlying theories and corresponding equations are explained in great detail in previous works (Prakash, Gunduz, et al., 2019b).

5.2.2 Material Model

In previous works, the constitutive behavior of the materials was modeled using a large deformation isotropic viscoplastic flow rule, however, in this work anisotropic parameters are used. The viscoplastic behavior of the materials are modeled via the constitutive stress-strain-strain rate viscoplastic power law:

$$\bar{\sigma} = F_0 \left(\frac{\dot{\bar{\epsilon}}^{vp}}{\dot{\bar{\epsilon}}^0} \right)^m (\bar{\epsilon}^{vp})^n \quad (2)$$

Where $\bar{\sigma}$ is the effective stress, $\bar{\varepsilon}^{vp}$ the effective viscoplastic strain, and $\dot{\bar{\varepsilon}}^{vp}$ the viscoplastic strain rate. $\dot{\bar{\varepsilon}}^0$ is a reference strain rate assumed to be 1s^{-1} . The stress and strain are obtained through small-scale dynamic impact experiments wherein the material is impacted at different strain rates by an impactor with a radius of $1\text{ }\mu\text{m}$. The model parameters F_0 , m , and n are then obtained by fitting Eq. (2). For HMX in this work, the model parameters were obtained for 3 miller planes and are displayed, along with the parameters for other materials, in Table 1 below.

Table 5.3. Anisotropic viscoplastic parameters

Material	F_0	m	n
HTPB	1.41	0.1	0.56
HMX-010	0.46	1.17	0.33
HMX-110	0.11	2.1	0.59
HMX-011	0.21	1.83	0.27
Polycrystal	0.95	0.5	0.63

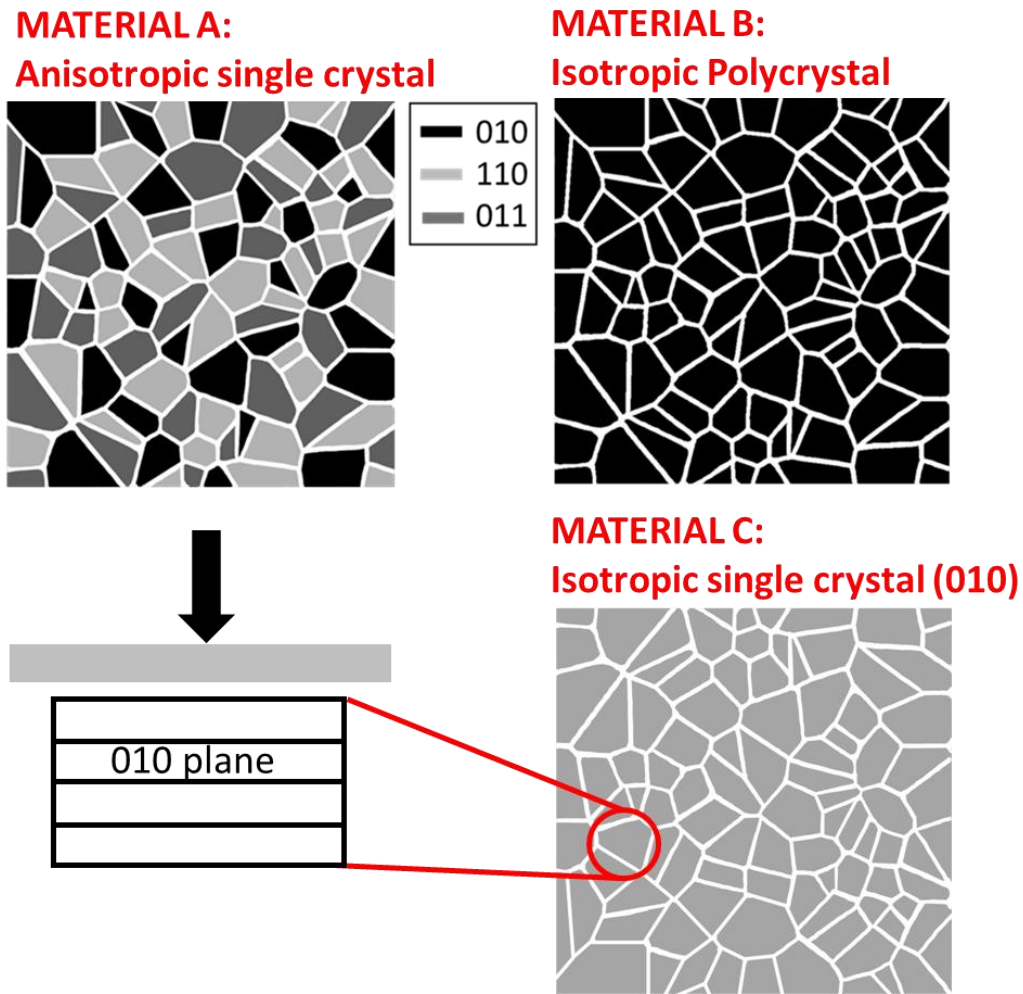


Figure 5.2. Microstructure for a) isotropic material property model of HMX particles b) anisotropic material property model

The material setup for the microstructure includes three variations of material orientation. The anisotropic microstructure involves random placed crystals corresponding to three different orientations throughout the microstructure. These crystals are then assigned a respective material property from the previously obtained anisotropic material properties listed in Table 5.1. Figure 5.2a shows the general schematic of the material distributions. The microstructure is modeled as locally isotropic, that is each particle is assigned an isotropic material property depending on the assigned orientation. For the isotropic microstructure, all crystals are the same orientation. All

materials had the same mesh sizes and boundary and loading conditions shown in Figure 5.1, including the impact velocity, which was set to 4.5 m/s for all microstructures. The orientations indicated imply that the crystals are assumed to be oriented with the specified plane perpendicular to the load. The microstructure is modeled to be 60,000 μm^2 with an element size of 4 μm .

5.3 Results and Discussion

Previous works have covered the microstructural behavior of isotropic polycrystalline PBX (A. Olokun et al., 2019). Here, we first observed the microstructural behavior of the anisotropic PBX material, shown in Figure 5.3. The material profile has been overlayed on the stress map for clarity. The stress wave can clearly be seen propagated through the material and reflected at the particle-binder interfaces, where the stresses build up and form concentrations as expected (A. Olokun et al., 2019). The overall stress distribution is not even across the top and bottom of the microstructure despite both impact velocities being equal. This is attributed to the different particle size distributions along the top and bottom of the microstructure as there is no symmetry. The top portion of the generated microstructure has larger particle sizes on average and as a result, there are less interfaces. The stress wave appears to propagate more freely through the 010 and 110 oriented crystals, whereas the interfacial stress concentrations appear to occur more frequently at borders of the 011 crystal.

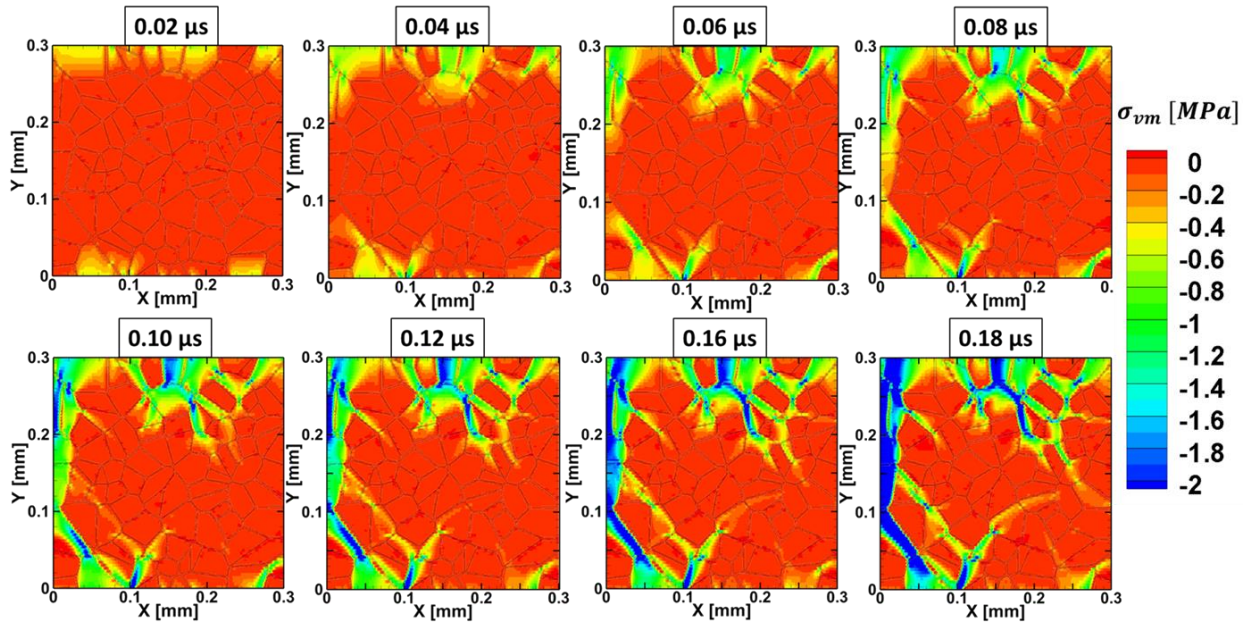


Figure 5.3 Progressive von mises stress profile of anisotropic material at different time steps

The pressure profile with time is compared for the anisotropic model and the isotropic model in Figure 5.4 below. Here, we can see a more even distribution of stress across the top and bottom of the isotropic microstructure. The isotropic microstructure also displayed generally higher stresses on average, also building up mostly in the particle-binder interfaces. The wave propagation speeds appear to be fairly similar for both microstructures at approximately 3km/s from the top surface and 1.5km/s from the bottom.

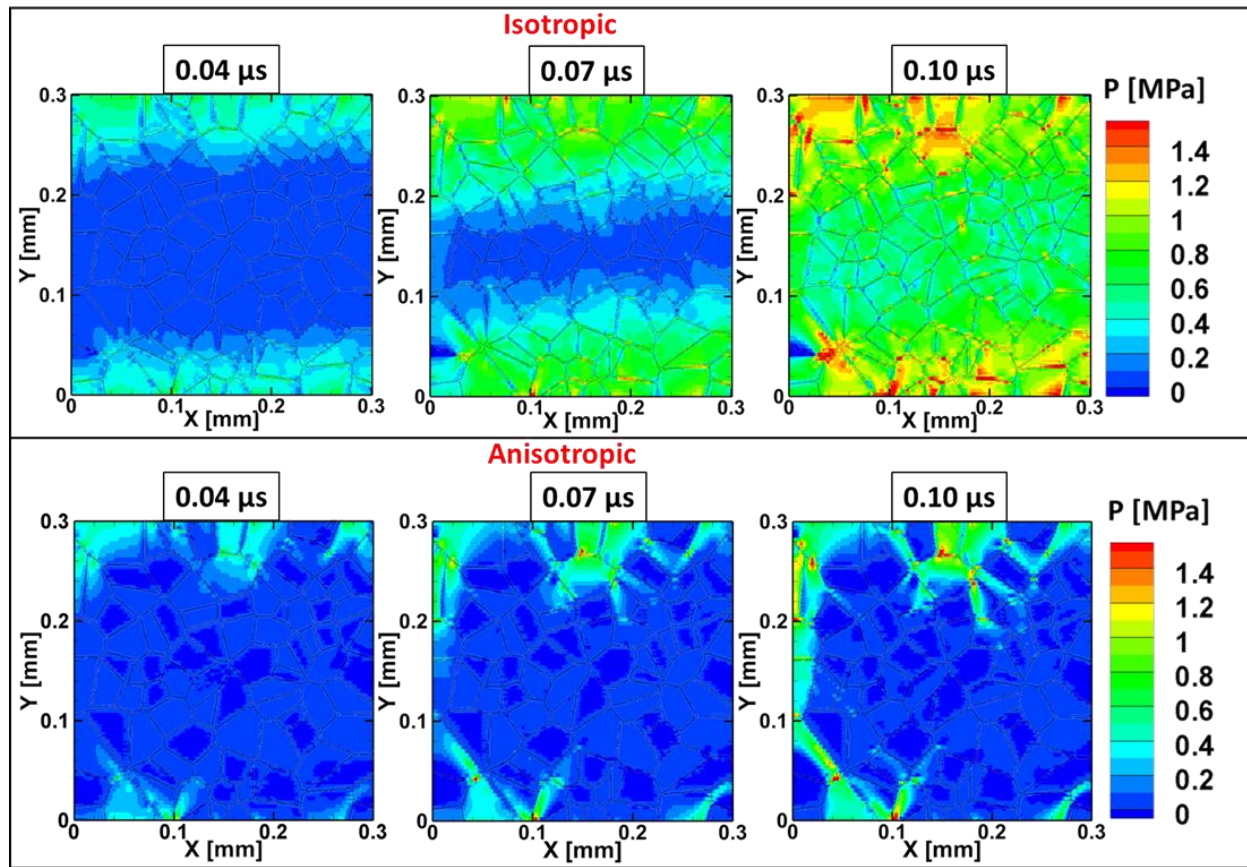


Figure 5.4. Pressure profile comparisons for isotropic and anisotropic microstructure

Observation of both materials in comparison at early stages shows similar stress distributions before the branching becomes prominent in the anisotropic model. Shown in Figure 5.5, the comparison of stress distributions also shows the uneven distribution of stress in differently oriented crystals. In Figure 5.6, the stress distribution of both isotropic microstructures are compared. The stress distributions are identical however, the microstructure with polycrystal material properties (Material B) had a lower maximum stress. This is attributed to the experimentally measured material properties.

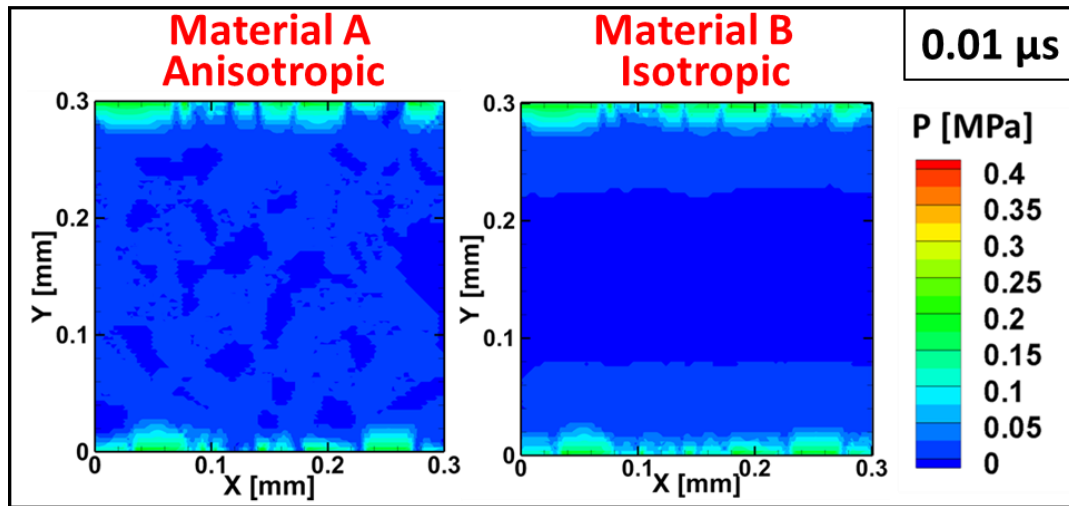


Figure 5.5. Early-stage stress distribution comparison between anisotropic and isotropic materials

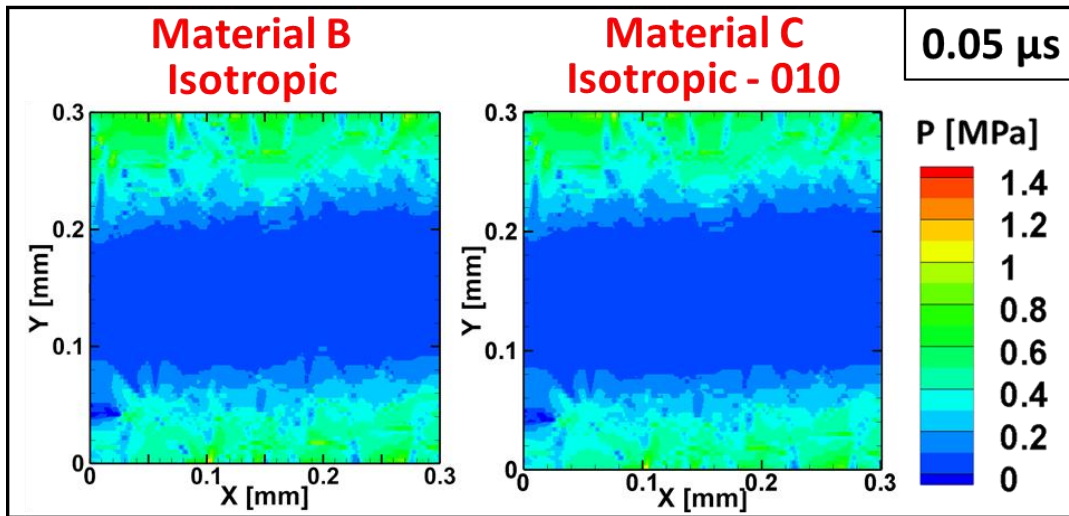


Figure 5.6. Stress distribution comparison between isotropic materials

Comparison of stress-time profiles of a specific particle in both anisotropic and isotropic microstructures reveals oscillatory behavior in the stress values for the anisotropic microstructure. Further investigation shows this to be the case for different This may explain the overall

deformation resistance of the material as the same stresses are reached in the anisotropic microstructure in twice the time of the isotropic material.

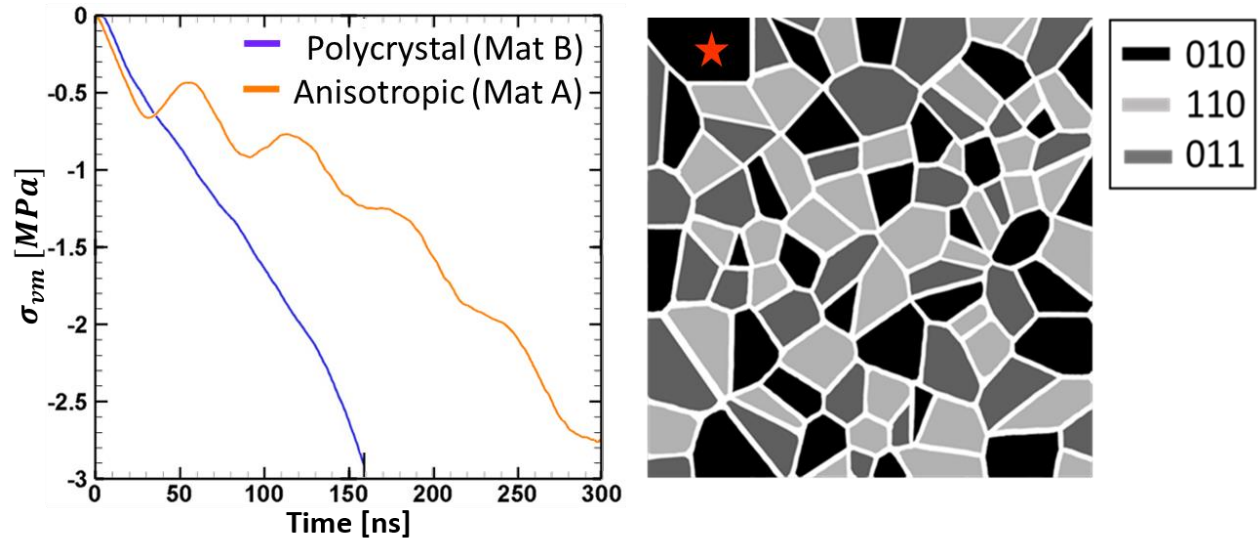


Figure 5.7. Particle level comparison of stress-time profile between anisotropic and isotropic materials

This is speculated to be due to the increased number of interfaces corresponding to material boundaries and selective stress propagation paths. However, the underlying mechanisms causing this phenomenon are yet to be fully understood as Figure 5.8 shows the stress wave velocity to be relatively unhindered at the times oscillatory behavior is noted.

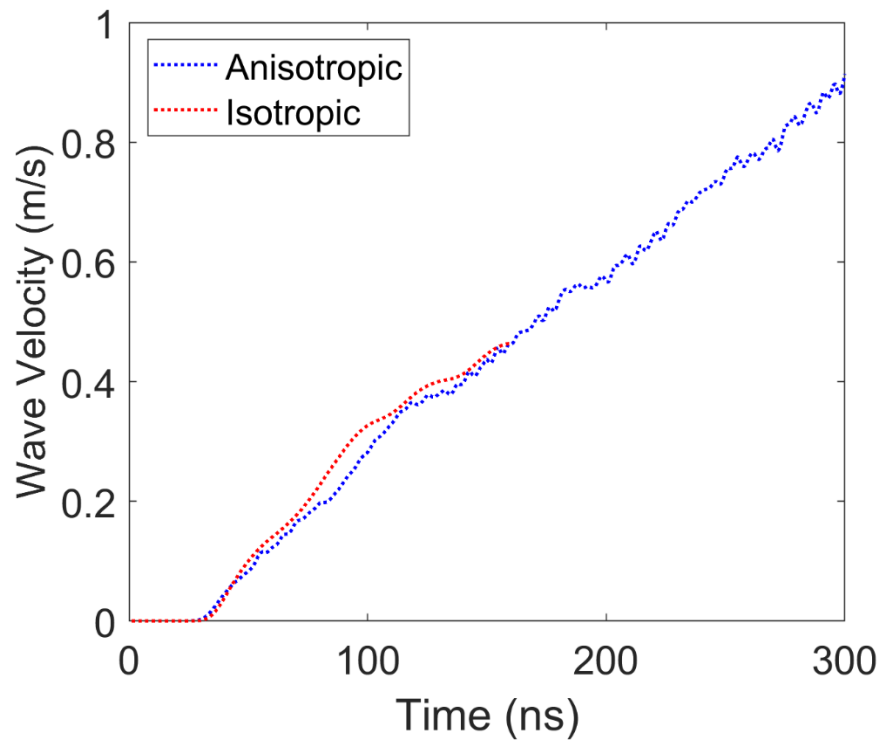


Figure 5.8. Stress particle wave velocity-time profile comparisons for anisotropic and isotropic materials

The maximum values of pressure and shear stress are plotted against time in Figures 5.8 and 5.9. The plots show that although the pressures for both microstructures were similar, the maximum shear stresses for the anisotropic microstructure were significantly higher. It is speculated that this is due to the interaction between the differently oriented particles. The isotropic microstructure reached very high mesh deformations quite quickly, while the anisotropic microstructure withstood much higher stresses for a longer period of time. This may merely be due to the material properties of the polycrystal material; however this may also imply that the anisotropic material interfaces result in a stronger material.

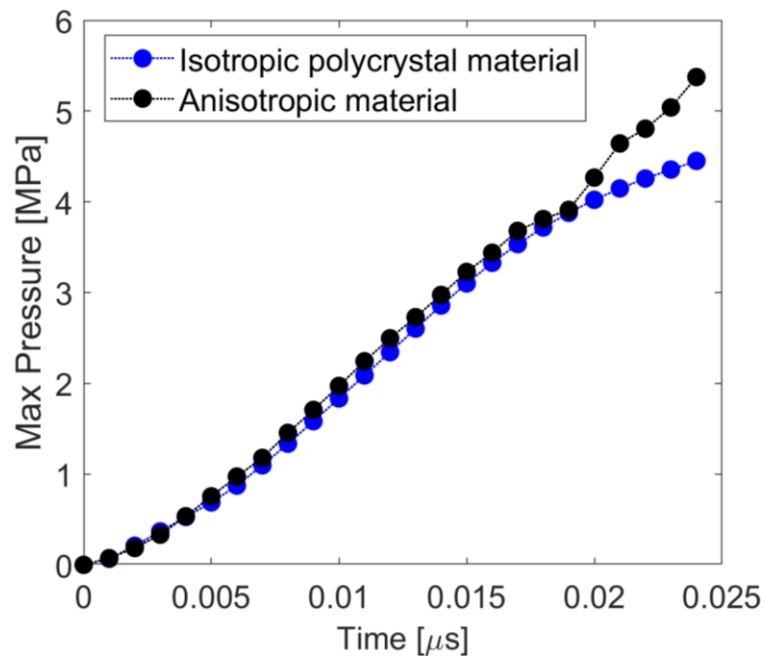


Figure 5.9. Maximum pressure vs time comparison for isotropic and anisotropic microstructure

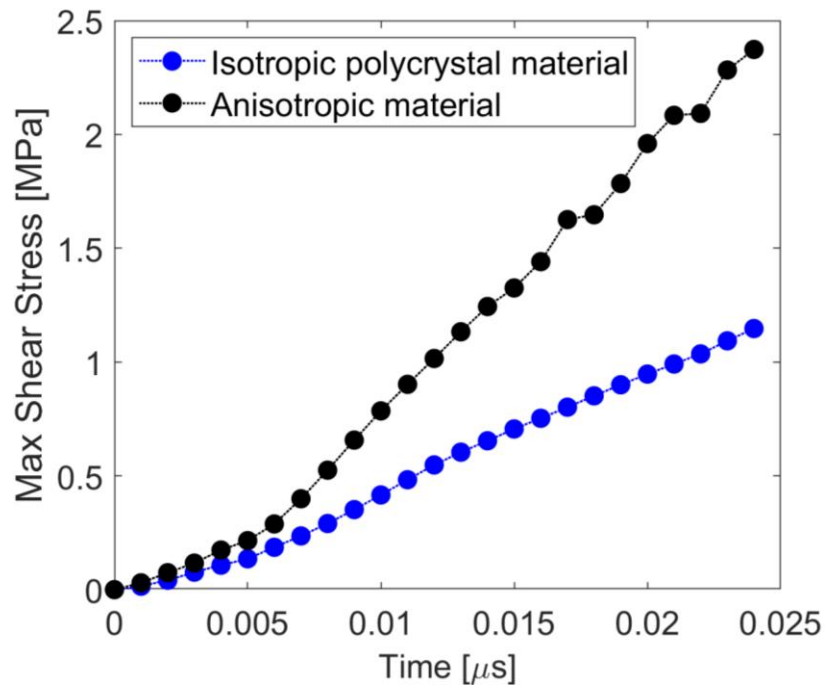


Figure 5.10. Maximum shear stress vs time comparison for isotropic and anisotropic microstructure

Shear stresses are a significant cause of delamination in composite materials and as such, the anisotropic model may be more efficient at particle-matrix delamination to even out high stress concentrations.

5.4 Conclusions

In this work, the numerical results of impact loaded microstructure containing anisotropic and isotropic HMX particles were compared. CFEM models were generated of both material models and impact simulated on top and bottom surfaces of the microstructure. The anisotropic material model exhibited selective faster wave propagation through 010 and 110 oriented crystals, which were predicted to have higher deformation resistance, and high stress concentrations at interfaces, particularly those involving the 011 oriented crystals. The average distributed stresses were higher in the isotropic material model however, the absolute maximum stresses were significantly higher for the anisotropic microstructure. Although shear stresses were high, the anisotropic model displayed more damage resistance than the isotropic model. This could be considered when determining safety factors for the EM such as fracture margins, as overestimation of damage conditions could lead to inefficient use of resources.

6. SUMMARY AND CONCLUSIONS

6.1 Summary

This work presents findings in the combined experimental and computational study of the effects of anisotropy and microstructure on the behavior of HMX-based energetic materials. Large single crystal samples of β -HMX were meticulously created by solvent evaporation for experimental purposes, and respective orientations were identified via x-ray diffraction. Nanoindentation methods were employed to describe anisotropic constitutive behaviors of the crystal. Small-scale dynamic impact experiments were carried out, and a viscoplastic power law model fit, to describe the anisotropic viscoplastic properties of the crystal. Indentation-nucleated crack system formations were studied in order to describe anisotropic fracture properties of the crystal, and two models for calculating fracture toughness were compared to obtain the values. Drop hammer impact tests were performed to investigate effects of morphology on the thermal response of HMX when impacted. Finally, the anisotropic properties obtained in this work were applied in a cohesive finite element simulation involving the impact of a sample of PBX containing HMX crystals with varying orientations. The results of this simulation were compared to those of simulation using isotropic properties of polycrystals under the same loading and boundary conditions and the observations were presented. Some findings from this work include:

1. Indentation modulus and hardness values were obtained for different orientations of β -HMX via nanoindentation experiments. Results obtained fit reasonably into a statistically determined range of values obtained from both numerical and experimental methods presented in literature. Values obtained for indentation moduli came particularly close to theoretical values of elastic moduli presented in literature.

2. The anisotropic fracture toughness and surface energy of β -HMX were calculated by fitting indentation load and crack length data to two different models, developed by Lawn and Laugier, and compared. We found the Lawn model to produce more satisfactory results which closely matched those presented in literature. It was found that the $\{011\}$ and $\{110\}$ planes had the highest and lowest fracture toughnesses respectively.
3. The drop hammer impact experiments on samples with varying crystal distance and sizes were performed and showed temperature spikes to occur where the crystals are in closer proximity. This matched the results from previous experimental and numerical analysis.
4. CFEM models were generated of microstructure containing both anisotropic and isotropic material models and impact simulated on top and bottom surfaces of the models. The anisotropic material exhibited higher deformation resistance and stress oscillations within particles, while the isotropic model had more even distributions of stress through the material. However, further work needs to be done to definitively draw conclusions concerning the necessity of anisotropy in modeling material composites such as PBXs.

6.2 Assumptions and Limitations

Some limitations and assumptions that may have influenced the results obtained in this work include:

1. Isotropic relations for finding indentation modulus and hardness were used on indentations in varying directions to obtain anisotropic values. This implies the possibility of uneven sub-surface elastic forces was neglected.
2. Surface cracks developed on some indentations, however through visual inspection under a microscope, it was determined that the cracks did not extend below the surface for

indentation moduli measurements. As the possibility of sub-surface cracking exists, moduli measured in this work were not labelled as elastic.

3. The imaging cameras used in this work had limited areas of acquisition and as such, hot spots may have occurred outside of the acquisition areas in some cases. As these hotspots could not be monitored, there exists the possibility of other unrecorded factors affecting the hot spot generation.
4. The CFEM framework used in this work assumed plane strain and isotropic cohesive properties. The model also functioned under the assumption of local isotropy which may not present the complete anisotropic details.

7. FUTURE WORK

The research in this work has created a basis in understanding the extent of anisotropy in elastic and plastic behaviors of β -HMX. The relatively wide ranges of values in the properties measured explains the variation in experimentally measured HMX behavior and highlights the necessity of incorporating anisotropic considerations when predicting the material's behavior. It has also shed light on some morphological effects on HMX microstructural responses to stress wave propagation and reflection. Detailed below are some planned and proposed future work in this area:

1. Additional experiments will need to be performed on other planes of β -HMX to complete the anisotropic material information. This will ensure robustness of the models and broaden the modeling accuracy.
2. Drop hammer impact experiments with curated but randomly oriented single crystal samples are planned to further add insight into the anisotropic thermomechanical response and macroscale behavior of HMX. The results of these experiments will also be incorporated into the CFEM model temperature computations.
3. Future simulations under different FEM frameworks are necessary to understand the effects of assumptions such as plane strain and plane stress. Also to further include microstructural effects such as anisotropic fracture properties and morphological parameters into the modeling of PBX materials. These may provide a basis of explanation

and/or validation of the oscillatory stress phenomena measured in some particles of the anisotropic material.

4. Further experimentation on thermal response is necessary to study the various effects of high strain rate induced temperature effects such as combustion and melting. These will affect the material's constitutive behavior, from which temperature dependent properties can be obtained to be included in the constitutive model.

PUBLICATIONS

Book Chapters

1. Prakash, C., **Olokun A.**, Emre Gunduz I., Tomar V., *Interface Mechanical Properties in Energetic Materials Using Nanoscale Impact Experiment and Nanomechanical Raman Spectroscopy*. In: Bhattacharya S., Agarwal A., Rajagopalan T., Patel V. (eds) NanoEnergetic Materials. Energy, Environment, and Sustainability. Springer, Singapore, 2019.

Journal Articles

1. **Olokun, A.**, Li, B., Prakash, C., Men, Z., Dlott, D. D., & Tomar, V., *Examination of Local Microscale-Microsecond Temperature Rise in HMX-HTPB Energetic Material Under Impact Loading*. JOM, 2019. **71**(10): p. 3531-3535.
2. **Olokun, A.**, Prakash, C., Emre Gunduz, I., & Tomar, V. (2020). *The role of microstructure in the impact induced temperature rise in hydroxyl terminated polybutadiene (HTPB)–cyclotetramethylene-tetranitramine (HMX) energetic materials using the cohesive finite element method*. Journal of Applied Physics, 128(6), 065901.
3. **Olokun, A.**, Dhiman, A., & Tomar, V. (Submitted, under review). *Experimental Measurements of Anisotropic Constitutive Behavior of β -HMX Crystals*. Propellants, Explosives, Pyrotechnics.
4. Dhiman, A., **Olokun, A.**, & Tomar, V. (2021). *Microscale Analysis of Stress Wave Propagation Through Plastic Bonded Explosives Under Micro-Sphere Shock Impact*. *Journal of Dynamic Behavior of Materials*.

Conference Proceedings

1. **Olokun, A.**, Prakash, C., Emre Gunduz, I., & Tomar, V. (2019, 2019//). *Interface Chemistry Dependent Mechanical Properties in Energetic Materials Using Nano-Scale Impact Experiment*. Paper presented at the Dynamic Behavior of Materials, Volume 1, Cham

REFEENCES

- Amuzu, J. K. A., Briscoe, B. J., & Chaudhri, M. M. (1976). Frictional properties of explosives. *Journal of Physics D: Applied Physics*, 9(4), 677-677. doi:10.1088/0022-3727/9/4/518
- Baer, M. R. (2002). Modeling heterogeneous energetic materials at the mesoscale. *Thermochimica Acta*, 384(1), 351-367. doi:https://doi.org/10.1016/S0040-6031(01)00794-8
- Barua, A., Horie, Y., & Zhou, M. (2012). Energy localization in HMX-Estane polymer-bonded explosives during impact loading. *Journal of Applied Physics*, 111(5), 054902. doi:10.1063/1.3688350
- Barua, A., Kim, S. P., Horie, Y., & Zhou, M. (2014). Computational Analysis of Ignition in Heterogeneous Energetic Materials. *Materials Science Forum*, 767, 13-21. doi:10.4028/www.scientific.net/MSF.767.13
- Benson, D. J., & Conley, P. (1999). Eulerian finite-element simulations of experimentally acquired HMX microstructures.
- Benson, D. J., & Conley, P. (1999). Eulerian finite-element simulations of experimentally acquired HMX microstructures. *Modelling and Simulation in Materials Science and Engineering*, 7(3), 333-354. doi:10.1088/0965-0393/7/3/304
- Burch, A., Yeager, J., & Bahr, D. (2017). Nanoindentation of HMX and Idoxuridine to Determine Mechanical Similarity. doi:10.3390/cryst7110335
- Conroy, M. W., Oleynik, I. I., Zybin, S. V., & White, C. T. (2008). First-principles anisotropic constitutive relationships in β -cyclotetramethylene tetranitramine (β -HMX). *Journal of Applied Physics*, 104(5), 053506. doi:10.1063/1.2973689

- Dai, K., Lu, B., Chen, P., & Chen, J. (2019). Modelling Microstructural Deformation and the Failure Process of Plastic Bonded Explosives Using the Cohesive Zone Model. *Materials*, 12(22). doi:10.3390/ma12223661
- Dick, J. J., Hooks, D. E., Menikoff, R., & Martinez, A. R. (2004). Elastic–plastic wave profiles in cyclotetramethylene tetranitramine crystals. *Journal of Applied Physics*, 96(1), 374-379. doi:10.1063/1.1757026
- Drodge, D. R., & Proud, W. G. (2009). THE EFFECTS OF PARTICLE SIZE AND SEPARATION ON PBX DEFORMATION. *AIP Conference Proceedings*, 1195(1), 1381-1384. doi:10.1063/1.3295067
- Dukino, R. D., & Swain, M. V. (1992). Comparative Measurement of Indentation Fracture Toughness with Berkovich and Vickers Indenters. *Journal of the American Ceramic Society*, 75(12), 3299-3304. doi:https://doi.org/10.1111/j.1151-2916.1992.tb04425.x
- Fan, Z., Swadener, J. G., Rho, J. Y., Roy, M. E., & Pharr, G. M. (2002). Anisotropic properties of human tibial cortical bone as measured by nanoindentation. *Journal of Orthopaedic Research*, 20(4), 806-810. doi:https://doi.org/10.1016/S0736-0266(01)00186-3
- Field, J. E. (1992). Hot spot ignition mechanisms for explosives. *Accounts of Chemical Research*, 25(11), 489-496. doi:10.1021/ar00023a002
- Gallagher, H. G., Sherwood, J. N., & Vrcelj, R. M. (2014). Growth and dislocation studies of β -HMX. *Chemistry Central Journal*, 8(1), 75. doi:10.1186/s13065-014-0075-y
- Harris, J., United, S., & National Technical Information, S. (1982). *Friction sensitivity of primary explosives*. Springfield, Va.: U.S. Dept. of Commerce, National Technical Information Service.

- Hooks, D. E., Ramos, K. J., Bolme, C. A., & Cawkwell, M. J. (2015). Elasticity of Crystalline Molecular Explosives. *Propellants, Explosives, Pyrotechnics*, 40(3), 333-350.
doi:<https://doi.org/10.1002/prop.201400282>
- Kucheyev, S. O., Gash, A. E., & Lorenz, T. (2014). Deformation and fracture of LLM-105 molecular crystals studied by nanoindentation. *Materials Research Express*, 1(2), 025036. doi:10.1088/2053-1591/1/2/025036
- Laugier, M. T. (1987). New formula for indentation toughness in ceramics. *Journal of Materials Science Letters*, 6(3), 355-356. doi:10.1007/BF01729352
- Lawn, B. R., & Fuller, E. R. (1975). Equilibrium penny-like cracks in indentation fracture. *Journal of Materials Science*, 10(12), 2016-2024. doi:10.1007/BF00557479
- Leitner, A., Maier-Kiener, V., & Kiener, D. (2017). Extraction of Flow Behavior and Hall–Petch Parameters Using a Nanoindentation Multiple Sharp Tip Approach *Advanced Engineering Materials*, 19(4), 1600669. doi:<https://doi.org/10.1002/adem.201600669>
- Li, M., Tan, W.-J., Kang, B., Xu, R.-J., & Tang, W. (2010). The Elastic Modulus of β -HMX Crystals Determined by Nanoindentation. *Propellants, Explosives, Pyrotechnics*, 35(4), 379-383. doi:<https://doi.org/10.1002/prop.201000018>
- Marsh, J., Han, Y. S., Verma, D., & Tomar, V. (2015). An investigation into plastic deformation of irradiated tungsten microstructure at elevated temperatures using the Anand's viscoplastic model. *International Journal of Plasticity*, 74, 127-140.
- Men, Z., Bassett, W., Suslick, K., & Dlott, D. (2018). Drop hammer with high-speed thermal imaging. *Review of Scientific Instruments*, 89, 115104. doi:10.1063/1.5051357

- Nix, W. D., & Gao, H. (1998). Indentation size effects in crystalline materials: A law for strain gradient plasticity. *Journal of the Mechanics and Physics of Solids*, 46(3), 411-425.
doi:[https://doi.org/10.1016/S0022-5096\(97\)00086-0](https://doi.org/10.1016/S0022-5096(97)00086-0)
- Oliver, W. C., & Pharr, G. M. (1992). An improved technique for determining hardness and elastic modulus using load and displacement sensing indentation experiments. *Journal of Materials Research*, 7(6), 1564-1583. doi:10.1557/JMR.1992.1564
- Olokun, A., Prakash, C., Emre Gunduz, I., & Tomar, V. (2019, 2019//). *Interface Chemistry Dependent Mechanical Properties in Energetic Materials Using Nano-Scale Impact Experiment*. Paper presented at the Dynamic Behavior of Materials, Volume 1, Cham.
- Olokun, A. M., Prakash, C., Emre Gunduz, I., & Tomar, V. (2020). The role of microstructure in the impact induced temperature rise in hydroxyl terminated polybutadiene (HTPB)–cyclotetramethylene-tetranitramine (HMX) energetic materials using the cohesive finite element method. *Journal of Applied Physics*, 128(6), 065901. doi:10.1063/5.0011264
- Palmer, S. J. P., & Field, J. E. (1982). The Deformation and Fracture of β -HMX. *Proceedings of the Royal Society of London. Series A, Mathematical and Physical Sciences*, 383(1785), 399-407. Retrieved from www.jstor.org/stable/2397290
- Pereverzev, A., & Sewell, T. (2020). Elastic Coefficients of β -HMX as Functions of Pressure and Temperature from Molecular Dynamics. *Crystals*, 10(12). doi:10.3390/cryst10121123
- Prakash, C., Emre Gunduz, I., & Tomar, V. (2018, 2018//). *Effect of Strain Rate and Interface Chemistry on Failure in Energetic Materials*. Paper presented at the Fracture, Fatigue, Failure and Damage Evolution, Volume 7, Cham.

- Prakash, C., Gunduz, I. E., Oskay, C., & Tomar, V. (2018). Effect of interface chemistry and strain rate on particle-matrix delamination in an energetic material. *Engineering Fracture Mechanics*, 191, 46-64. doi:<https://doi.org/10.1016/j.engfracmech.2018.01.010>
- Prakash, C., Gunduz, I. E., & Tomar, V. (2019a). The effect of interface shock viscosity on the strain rate induced temperature rise in an energetic material analyzed using the cohesive finite element method. *Modelling and Simulation in Materials Science and Engineering*, 27(6), 065008. doi:10.1088/1361-651x/ab2224
- Prakash, C., Gunduz, I. E., & Tomar, V. (2019b). Simulation guided experimental interface shock viscosity measurement in an energetic material. *Modelling and Simulation in Materials Science and Engineering*, 27(8), 085003. doi:10.1088/1361-651x/ab4148
- Prakash, C., Olokun, A., Emre Gunduz, I., & Tomar, V. (2019). Interface Mechanical Properties in Energetic Materials Using Nanoscale Impact Experiment and Nanomechanical Raman Spectroscopy. In S. Bhattacharya, A. K. Agarwal, T. Rajagopalan, & V. K. Patel (Eds.), *Nano-Energetic Materials* (pp. 275-290). Singapore: Springer Singapore.
- Prakash, C., Olokun, A., Gunduz, I. E., & Tomar, V. (2019). Interface Mechanical Properties in Energetic Materials Using Nanoscale Impact Experiment and Nanomechanical Raman Spectroscopy. In S. Bhattacharya, A. K. Agarwal, T. Rajagopalan, & V. K. Patel (Eds.), *Energy, Environment, and Sustainability*: Springer, Singapore.
- Rae, P. J., Hooks, D., & Liu, C. (2006). The stress versus strain response of single β -HMX crystals in quasi-static compression. *Proceedings of the 13th International Detonation Symposium, IDS 2006*, 293-301.

- Rae, P. J., Palmer, S. J. P., Goldrein, H. T., Field, J. E., & Lewis, A. L. (2002). Quasi-static studies of the deformation and failure of PBX 9501. *Proceedings of the Royal Society of London. Series A: Mathematical, Physical and Engineering Sciences*, 458(2025), 2227-2242. doi:10.1098/rspa.2002.0967
- S.J.P, P., J.E., F., & J.M., H. (1993). Deformations, strength and strains to failure of Polymer Bonded Explosives.
- Sakharova, N. A., Fernandes, J. V., Antunes, J. M., & Oliveira, M. C. (2009). Comparison between Berkovich, Vickers and conical indentation tests: A three-dimensional numerical simulation study. *International Journal of Solids and Structures*, 46(5), 1095-1104. doi:https://doi.org/10.1016/j.ijsolstr.2008.10.032
- Sewell, T. D., Menikoff, R., Bedrov, D., & Smith, G. D. (2003). A molecular dynamics simulation study of elastic properties of HMX. *The Journal of Chemical Physics*, 119(14), 7417-7426. doi:10.1063/1.1599273
- Sivabalan, R., Gore, G. M., Nair, U. R., Saikia, A., Venugopalan, S., & Gandhe, B. R. (2007). Study on ultrasound assisted precipitation of CL-20 and its effect on morphology and sensitivity. *Journal of hazardous materials*, 139(2), 199-203. doi:https://doi.org/10.1016/j.jhazmat.2006.06.027
- Stevens, L. L., & Eckhardt, C. J. (2005). The elastic constants and related properties of β -HMX determined by Brillouin scattering. *The Journal of Chemical Physics*, 122(17), 174701. doi:10.1063/1.1883627

- Sun, B., Winey, J. M., Gupta, Y. M., & Hooks, D. E. (2009). Determination of second-order elastic constants of cyclotetramethylene tetranitramine (β -HMX) using impulsive stimulated thermal scattering. *Journal of Applied Physics*, *106*(5), 053505. doi:10.1063/1.3211927
- Tan, H., Huang, Y., Liu, C., & Geubelle, P. H. (2005). The Mori–Tanaka method for composite materials with nonlinear interface debonding. *International Journal of Plasticity*, *21*(10), 1890-1918. doi:<https://doi.org/10.1016/j.ijplas.2004.10.001>
- Tandon, R., Marshall, D. B., Cook, R. F., Padture, N. P., Oyen, M. L., Pajares, A., . . . Lawn, B. R. (2015). The compelling case for indentation as a functional exploratory and characterization tool. doi:10.1111/jace.13729
- Verma, D., & Tomar, V. (2014). Structural-Nanomechanical Property Correlation of Shallow Water Shrimp (*Pandalus platyceros*) Exoskeleton at Elevated Temperature. *Journal of Bionic Engineering*, *11*(3), 360-370. doi:[https://doi.org/10.1016/S1672-6529\(14\)60049-4](https://doi.org/10.1016/S1672-6529(14)60049-4)
- Wang, D. D., Shu, Y. J., Li, M., Chen, T. N., Kang, B., & Song, M. X. (2011). Fracture toughness of RDX and HMX single-crystal by indentation. *Huozhayao Xuebao/Chinese Journal of Explosives and Propellants*, *34*, 28-31.
- Wang, H., Dhiman, A., Ostergaard, H. E., Zhang, Y., Siegmund, T., Kruzic, J. J., & Tomar, V. (2019). Nanoindentation based properties of Inconel 718 at elevated temperatures: A comparison of conventional versus additively manufactured samples. *International Journal of Plasticity*, *120*, 380-394. doi:<https://doi.org/10.1016/j.ijplas.2019.04.018>
- Wang, H., Thomas, J., Okuniewski, M. A., & Tomar, V. (2020). Constitutive modeling of δ -phase zircaloy hydride based on strain rate dependent nanoindentation and nano-scale impact dataset. *International Journal of Plasticity*, *133*, 102787.

- Wang, X., Wu, Y., & Huang, F. (2017). Numerical mesoscopic investigations of dynamic damage and failure mechanisms of polymer bonded explosives. *International Journal of Solids and Structures*, 129, 28-39. doi:<https://doi.org/10.1016/j.ijsolstr.2017.09.017>
- Zamiri, A., & De, S. (2011). Modeling the Anisotropic Deformation Response of β -HMX Molecular Crystals. *Propellants, Explosives, Pyrotechnics*, 36. doi:10.1002/prep.201000037
- Zaug, J. M. (1998, 1998-08-21). *Elastic constants of B-HMX and tantalum, equations of state of supercritical fluids and fluid mixtures and thermal transport determinations*, United States.
- Zhai, J., & Zhou, M. (2000). Finite element analysis of micromechanical failure modes in a heterogeneous ceramic material system. *International Journal of Fracture*, 101(1), 161-180. doi:10.1023/A:1007545105723
- Zhang, Y., Mohanty, D. P., Seiler, P., Siegmund, T., Kruzic, J. J., & Tomar, V. (2017). High temperature indentation based property measurements of IN-617. *International Journal of Plasticity*, 96, 264-281.